2018년 8월
박사학위 논문

Growth mechanism of Alq₃ via solution growth method with [C₁₂mim][TFSI] ionic liquid

조선대학교 대학원

첨단부품소재공학과

박 세 연

Growth mechanism of Alq$_3$ via solution growth method with [C$_{12}$mim][TFSI] ionic liquid

[C$_{12}$mim][TFSI] 이온성 액체 용액법으로 성장한 Alq$_3$ 결정성장 메커니즘

2018년 8월 24

조선대학교 대학원

첨단부품소재공학과

박 세 연

Growth mechanism of Alq$_3$ via solution growth method with [C$_{12}$mim][TFSI] ionic liquid

지도교수   신 동 찬

이 논문을 공학 박사학위신청 논문으로 제출함

2018년 4월

조선대학교 대학원

첨단부품소재공학과

박 세 연

박세연의 박사학위논문을 인준함

위원장 이 종 국   (인)

위 원 양 권 승   (인)

위 원 신 동 찬   (인)

위 원 이 종 원   (인)

위 원 이 종 호   (인)

2018년 6월

조선대학교 대학원

CONTENTS

LIST OF TABLES

LIST OF FIGURES

초록

[C₁₂mim][TFSI] 이온성 액체 용액법으로 성장한 Alq₃ 결정성장 메커니즘

박 세 연

지도교수 : 신 동 찬

첨단부품소재공학과

조선대학교 대학원

유기반도체는 분자 단위의 합성을 통해 다양한 응용분야의 요구에 적합하도록 제작할 수 있고 높은 유연성, 낮은 제작 단가, 용액공정을 통한 대면적 소자 제작 용이 등 차세대 전자소자 적용에 필요한 요소를 갖추고 있는 매력적인 재료이다. 그러나, 공유결합을 갖는 무기 반도체와 달리 van der waals 결합을 이루고 있는 유기 반도체는 전하 이동층이 불안정하고 주입된 전하가 주변 전자층과 반응하여 전하 이동에 제약을 받고 유기반도체 재료의 경우 분자구조가 amorphous 혹은 polycrystalline으로 되어 있어 전하가 hopping mechanism에 의해 이동하므로 전도도가 낮아 실제 소자 적용이 어렵다는 문제를 갖고 있다. 따라서 유기반도체 성능 향상을 위해서는 높은 전도도를 갖는 유기재료가 필요하므로 고순도 단결정 유기재료 제작이 필수적이다.

고순도 단결정 유기재료는 분자 구조 설계, 분자 배향 및 결정성을 제어하여 얻을 수 있다. 유기발광재료의 고순도화를 위해 현재 승화정제법이 사용되고 있다. 그러나 이 방법은 3 ~ 5회 이상 동일 공정의 반복을 통해 99.9% 이상 요구되는 순도를 얻을 수 있으므로 정제 수율이 낮고, 각 재료마다 공정 최적화 작업이 필요하고, 재료 수득 공정의 자동화가 어려워 인력이 투입되어야하는 등의 이유로 고순도 재료 제작을 위한 제조단가가 높은 문제점을 가지고 있다.

본 연구에서는 [C₁₂mim][TFSI] 이온성 액체를 용매로 사용한 용액법을 통해 OLED 대표 재료인 Alq₃ 결정성장에 대해 연구하였다. [C₁₂mim][TFSI] 이온성 액체와 Alq₃의 혼합용액을 열처리 온도와 조성에 따른 결정성장을 통해 얻은 Alq₃ 결

정을 분석한 결과 열처리 온도가 100℃에서 180℃로 증가할수록 성장모양에서 평형모양으로 바뀌며 XRD 측정 결과는 열처리 온도가 증가할수록 ɣ-phase에서 δ-phase로 상전이 되는 것을 확인하였다. 특히 16 mol% Alq_3를 180℃ 온도에서 결정성장 시킨 Alq_3의 경우 순수한 δ-phase을 얻을 수 있었다. [C_{12}mim][TFSI] 이온성 액체 내에서의 Alq_3 결정 성장 메커니즘은 열처리 공정 중 이온성 액체 내의 H^+ 이온 농도의 변화에 따라 hexagonal-rod의 단면이 우선 성장되는 결과로 hollow structure에서 hexagonal-rod로 결정이 성장되었다. 용액법으로 성장된 Alq_3 결정의 순도는 결정의 크기가 클수록 높아지므로 입자 조대화 조건을 탐색하였고 200℃ 열처리 온도에서 100℃까지 0.05℃/min의 냉각속도로 결정을 성장시킨 결과 176 ㎛ 크기의 Alq_3 결정을 얻었다. 이온성 액체를 용매로 사용한 용액법을 통해 단결정, 고순도 Alq_3의 대량생산 제작이 가능할 것이라 생각되며 이온성 액체 내에서의 Alq_3 결정성장 메커니즘 규명 연구를 통해 향후 관련 분야 학문 발전에도 기여할 수 있을 것이다.

I. INTRODUCTION

Organic semiconductors are attractive materials that can be designed to satisfy the needs of various applications through the synthesis of molecular units and have the features required for application to next-generation electronic devices such as high flexibility, low production cost, and ease of fabricating large-area devices through the solution process [1, 2]. As shown in Fig. 1, organic thin-film transistor, which is a flexible organic thin-film transistor produced using ink-jet printing with silver nano-particle ink, has been observed to have excellent durability under bending strain [3]. The organic light-emitting diode (OLED) display was first unveiled by LG in CES 2018, which consisted of 246 open-frame OLED displays and flexible substrates with a total length of 27 m. The power conversion efficiency of organic solar cells has been improved to 15% in 2017 [4]. Thus, organic semiconductors are being studied extensively and they are drawing attention as next-generation electronic devices.

However, unlike inorganic semiconductors, which have covalent bonds, organic semiconductors have van der Waals bonds. Thus, the charge transfer layer is unstable and charge transfer is restricted because the injected charge reacts with the nearby electron layer. Another problem of organic semiconductors is the difficulty of actual application to devices because the molecular structure of the material is amorphous or polycrystalline and the charge are moved by the hopping mechanism, resulting in low conductivity [5, 6]. Therefore, the production of a high-purity single-crystal organic material is essential as an organic material with high conductivity is required to improve the performance of organic semiconductors. This high-purity single-crystal organic material can be obtained by controlling the molecular structure design, molecular orientation, and crystallinity.

As shown in Fig. 2, a report published by UBI Research predicted that the OLED display market will more than quadruple from $8,716 million in 2017 to $38,210 million in 2021. Furthermore, the OLED material market is predicted to expand to $2,436 million in 2021 as shown in Fig. 3, of which emitting layers account for more than half. Furthermore, the analysis of OLED panel production cost in Fig. 4 shows

that the percentage of materials increases from 44% to 82% with the increase in panel size. Considering these data, it is critical to lower the cost of OLED material for the practical application of large-area OLED devices such as OLED TVs and lightings.
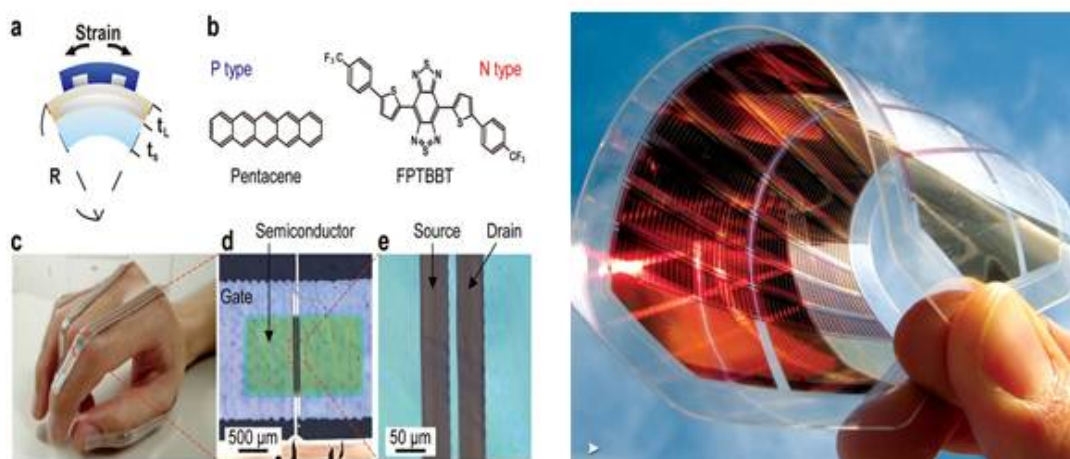
Fig. 2. Organic semiconductor. OLED (top), OTFT (left bottom), organic solar cell (right bottom).
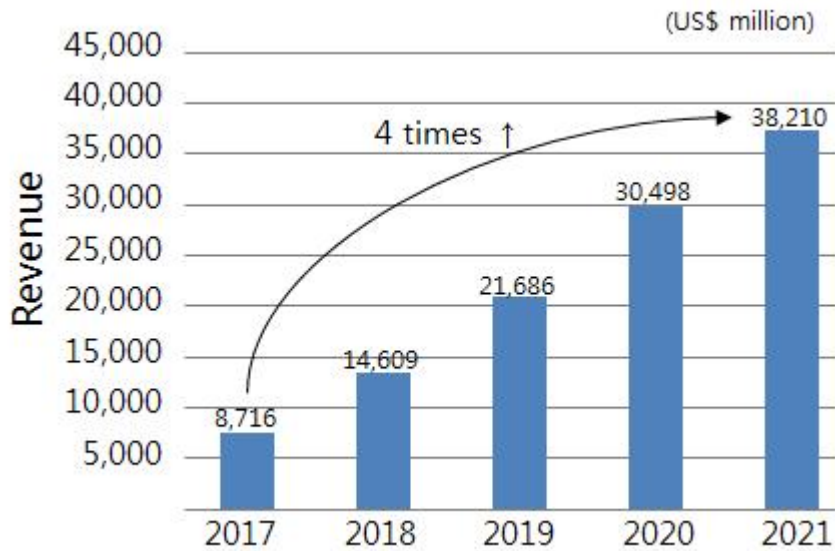
Fig. 3. OLED parts material market growth forecast.

[source : UBI Research 2017]
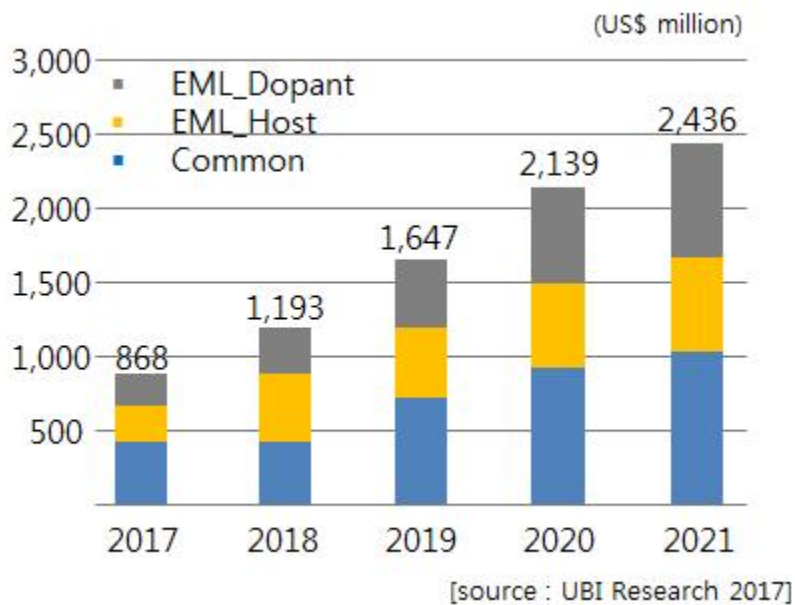
Fig. 4. OLED material revenues by type - all applications.
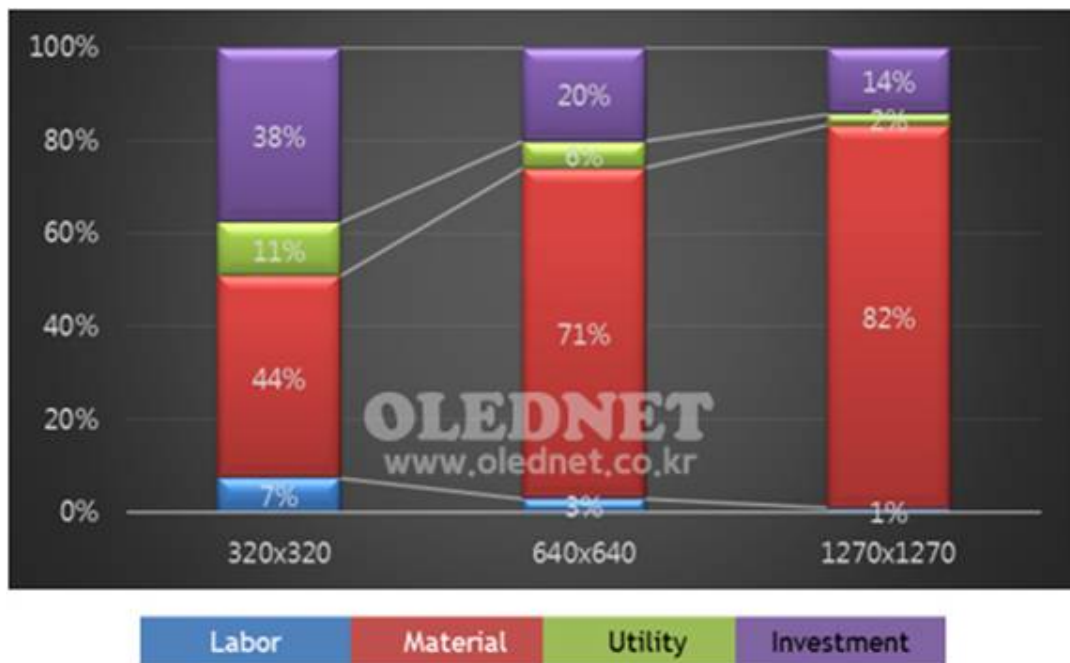
Fig. 5. Cost analysis of OLED panel.

To produce high-purity organic materials, the solution method using an organic solvent or the sublimation purification method is mainly used. Recrystallization of organic materials using an organic solvent is a simple process and facilitates mass production. However, it has the disadvantages that the crystalline quality of organic materials is lowered owing to the strong volatility of the organic solvent and the handling of most organic solvents is dangerous owing to toxicity and explosion risk. The sublimation purification method illustrated in Fig. 5 can be used to purify organic materials by using the difference in the sublimation points of organic materials. However, the purification yield is low because the same process must be repeated 3 ~ 5 times to obtain purity of 99.9% or higher, equipment optimization is required depending on the characteristics of organic materials, and manual work must be deployed because the material acquisition process is difficult to automate, resulting in a high production cost of high-purity materials. Thus, these limitations should be mitigated before the sublimation purification method can be introduced in the organic semiconductor industry. The solution method used in this study is a process of mixing the OLED material with a solvent and thereafter heating and cooling the mixed solution. It has advantages in that the equipment and process are simple, a high-purity OLED material can be produced in a single process, and mass production is easy because of high purification yield. Consequently, it is expected that the solution method can lower the cost of OLED materials to one eighth when compared with the cost incurred by the conventional sublimation purification method.
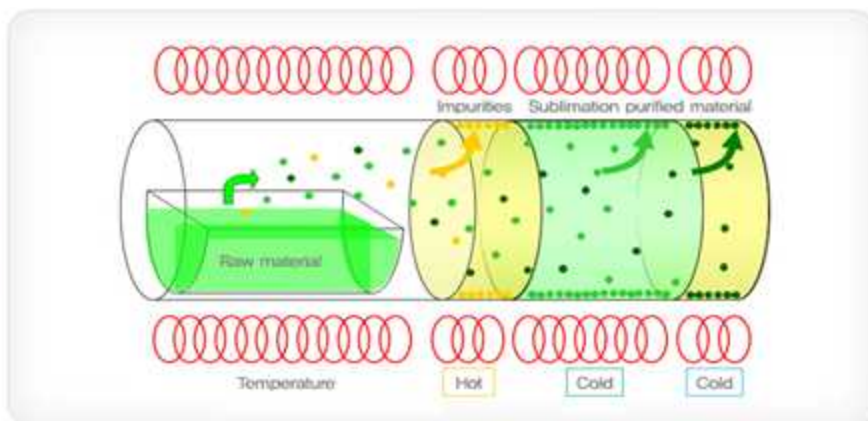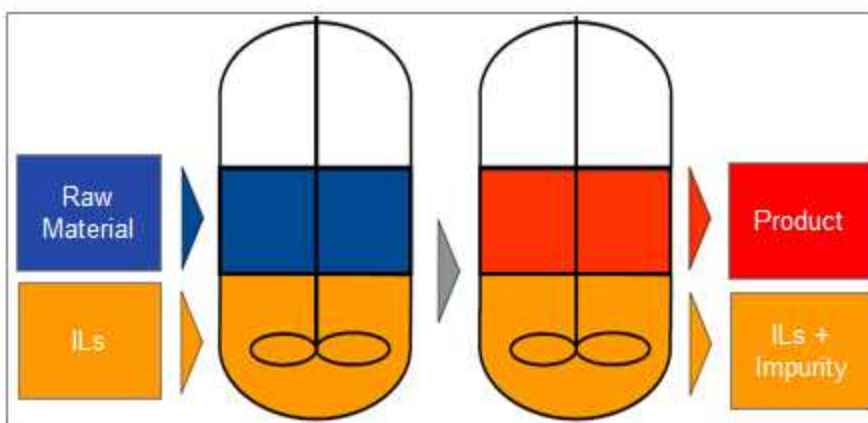
Fig. 6. A schematic diagram of a method for purifying OLED materials. Sublimation method (top), Solution method (bottom).

Studies have been conducted continuously to improve the characteristics of organic semiconductors by controlling the molecular structure design, molecular orientation, and crystallinity of organic materials used in organic semiconductors in order to produce organic semiconductors with high conductivity.

For example, it has been reported that the polymer semiconductor based on diketopyrrolopyrrole (DDP) shows a conductivity of 1 $cm^2/V·s$ at room temperature, but when zeta-branched alkyl chain was introduced, the conductivity increased more than 12 times owing to the reduction of distance between π-planes [7]. Furthermore, when a macroscopically oriented thin film was produced using the slow drying method with poly [4-(4,4-dihexadecyl-4H-cyclopenta [1,2-b:5,4-b']dithiophen-2-yl)-alt-[1,2,5]thiadiazolo[3,4-c]pyridine] (PCDTPT), it showed a conductivity of 23.7 $cm^2/V·s$, which is 30 times higher than that of polycrystalline, and when PCDTPT was produced by inducing self-assembly and unidirectional alignment, it showed a conductivity of 36.3 $cm^2/V·s$, which is close to the intrinsic conductivity (47 $cm^2/V·s$) [8, 9].

J. -S. Hu et al. measured the field-emission characteristics of an Alq_3 (Tris-8-(hydroxyquinoline)aluminum) nanorod produced using the solution method [10]. This Alq_3 nanorod showed a turn-on field of 3.1 V/μm and the maximum current density of approximately 1.38 mA/cm^2 in an applied field of 5.7 V/μm. Although the turn-on field was lower than those of other organic or inorganic nanomaterials, it was similar to that of organic charge-transfer complex nanowires. From these results, it is expected that the carrier mobility or conductivity of Alq_3 in nanowire form will be high and the characteristics of organic electronic devices using Alq_3 will be improved if Alq_3 of this form can be produced and its length and shape can be adjusted depending on the condition.

Our research group has been conducting research to improve the purity of OLED materials using ionic liquids for the past few years and we have acquired technology to obtain purity of 99.9% or higher through a process using the solution method with ionic liquids. A study published by Y. -T. Oh et al. early this year improved the purity of NPB (N,N'-Di-[(1-naphthyl)-N,N'-diphenyl]-1,1'-biphenyl-4,4'-diamine ($C_{44}H_{32}N_2$)) among the OLED materials. As shown in Fig. 6, the process of dissolution of NPB in the ionic liquid and its recrystallization was verified in situ, and as shown in Fig. 7, the high-performance liquid chromatography measurement to determine the purity of the recrystallized NPB shows that the purity improved from 82.375% at first to 99.921% after the entire process [11].

The present study analyzed the crystal growth mechanism of Alq_3, which is a typical light-emitting material of OLED devices. The crystals were grown through the solution method using an ionic liquid.
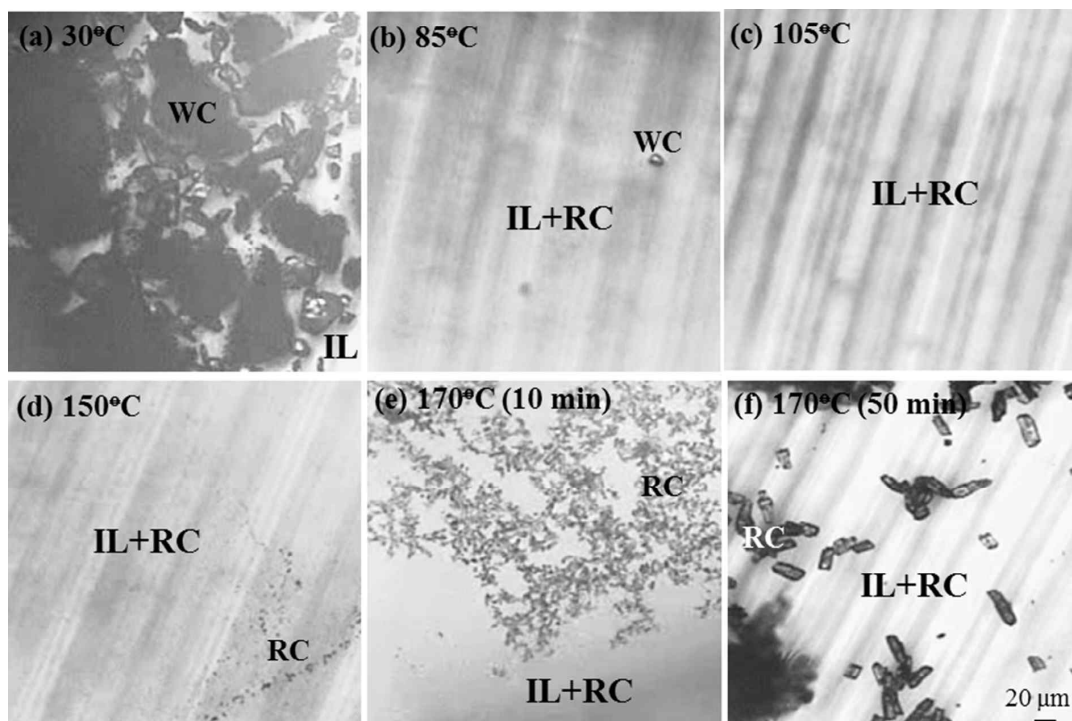
Fig. 7. Optical photograph showing dissolution and recrystallization behaviors of NPB crystal in [C$_4$mim][TFSI] during continuous heating (a ~ d) and isothermal heat-treatment at 170℃ for (e) 10 min and (f) 50 min [11].
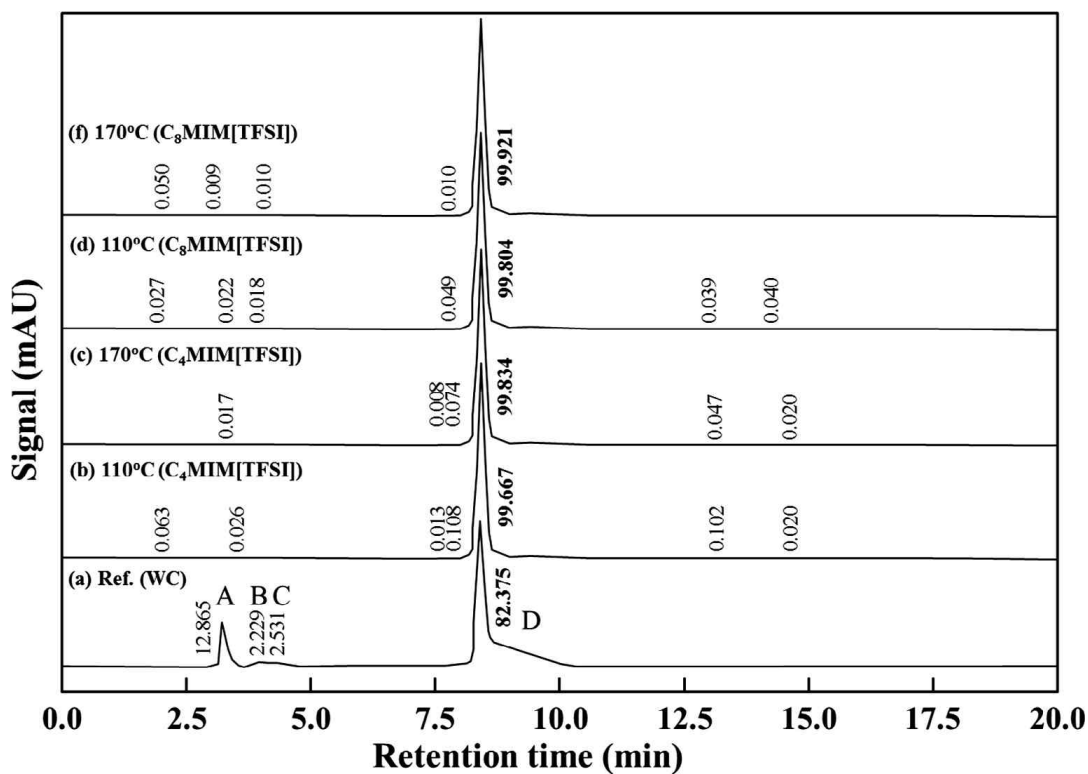
Fig. 8. HPLC results showing purity variation of RC (recrystallized NPB) crystal isothermally heat-treated at 110℃ and 170℃ for 1 h in [C₄mim][TFSI] and [C₈mim][TFSI] ionic liquids [11].

II. BACKGROUND

1. Nucleation [12]

Nucleation is a pure thermodynamic model that explains the process of the first step in a first order phase transition. It describes the appearance of a new phase - the nucleus - in the metastable primary phase. The vast majority of the available theoretical work on nucleation applying equilibrium thermodynamics is based on the classical nucleation theory developed by Becker and Döring more than 70 years ago. The classical nucleation theory applies that a thermodynamic system tends to minimize its Gibbs free energy (i.e. to maximize the entropy of the whole system).

Originally a thermodynamic approach describing the condensation of liquid from the vapor phase, it was extended to other types of phase transitions, thus making it an apparent ideal candidate for precipitation processes as well as crystallization of solids. This thermodynamic theory was also transferred to growth processes of nanoparticles such as LaMer's theory.

The concept of classical nucleation theory is based on the macroscopic Gibbs capillary effect, meaning that macroscopic entities such as the surface energy are taken to develop expressions for the nucleation rate. In this regard, it is important to distinguish between homogeneous and heterogeneous nucleation. Nucleation which occurs at nucleation sites on solid surfaces contacting the liquid or vapor is referred to as heterogeneous nucleation. Exemplarily, a heterogeneous nucleation in the field of nanoparticles growth occurs at the surface of particles in solution providing nucleation sites, used in seeded-growth syntheses. In contrast, homogeneous nucleation occurs spontaneously and randomly, but requires a supercritical state such as a supersaturation.
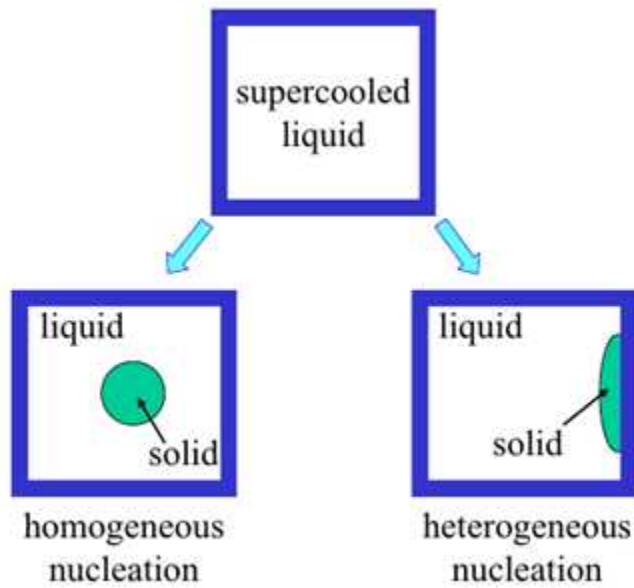
Fig. 9. Scheme of homogeneous nucleation and
heterogeneous nucleation.

1) Homogeneous nucleation

The Gibbs free energy of a nucleus is generally described as the sum of a positive and a negative term. The negative term indicates the desired binding energy between the monomer and the clusters and theoretically leads to a reduction in the Gibbs bulk free energy between the two monomers. The positive term describes how this combination of not desirable due to the increase in the Gibbs free surface energy. In its simplest form with spherical symmetry, the Gibbs free energy of a cluster (ΔG) is given as:

$$\triangle G = -\frac{4}{3}\pi r^3 \left| \triangle G_V \right| + 4\pi^2\gamma \qquad \text{eqn(1)}$$

with the radius r, the difference in Gibbs bulk free energy per unit volume $|\Delta G_V|$ and the surface energy per unit area ɣ. Due to the negative (bond making) and positive (surface energy) terms, the curve of the cluster Gibbs free energy displayed in Fig. 9 has a maximum at a radius r_c called the critical radius, so the energy barrier is called the activation energy ΔG_c. For clusters smaller than r_c, growth is unfavorable and dissolution is more probable. For clusters with a radius larger than r_c, growth is favored. The critical radius can easily be determined by solving eqn (1) for $d\Delta G/dr = 0$ leading to:

$$r_c = \frac{2\gamma}{\left| \triangle G_V \right|} \qquad \text{eqn (2)}$$

Substituting r in eqn (1) with r_c from eqn (2) yields the expression for the critical free energy ΔG_c:

$$\triangle G_c = \frac{16\pi\gamma^3}{\left| \triangle G_V \right|^2} \qquad \text{eqn (3)}$$

- 14 -

The nucleation rate J (T, ΔG_c) can be expressed using the Arrhenius equation since the energy barrier is an activation energy and thus nucleation a statistical process:

$$J(T, \triangle G_c) = A exp\left(\frac{-\triangle G_c}{\kappa_B T}\right)$$

eqn (4)
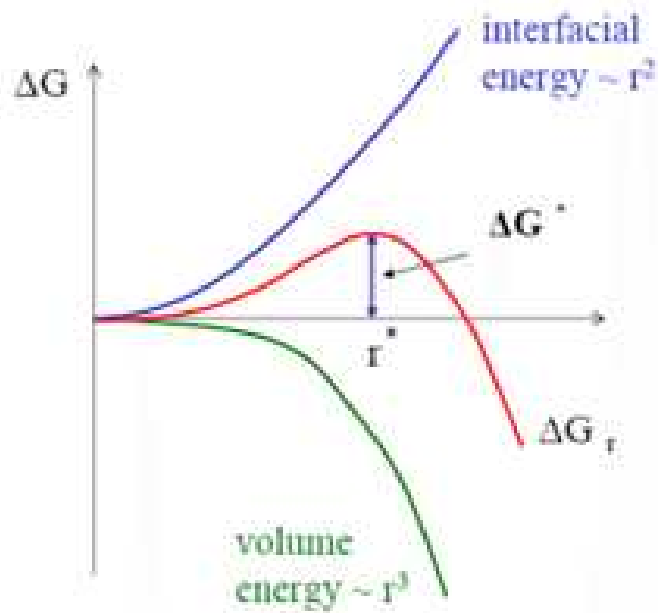
Fig. 10. The surface and volume contributions and the total excess free energy ΔG of spherical solid nucleus within a supercooled liquid as a function of the nucleus radius r.

2) **Heterogeneous nucleation**

Heterogeneous nucleation is referred to as nucleation at preferential sites of surfaces. The basic assumption is that the effective surface is low in the dominant region, such as the phase boundary or impurity, thereby reducing the activation energy. This makes nucleation at these preferential sites more possible. Therefor , heterogeneous nucleation happens more often than homogeneous nucleation. The driving force for successful seed-mediated growth in nanoparticles synthesis is heterogeneous nucleation. Nevertheless, it is assumed that in nanoparticles synthesis, two types of nucleation occur in succession and parallel.
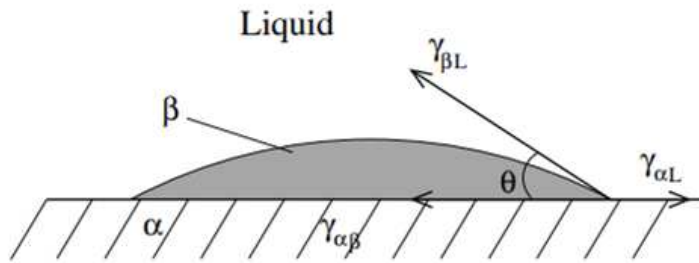
Fig. 11. Heterogeneous nucleation of spherical cap on a flat
mold wall [12].

2. Growth

1) Equilibrium shape [13]

In general, the particle shape is determined by two factors, equilibrium and growth forms (Elwell & Scheel, 1975). It has an equilibrium form when it has minimum surface free energy and can be represented by Wulff or γ plot. The Wulff plot is a polar diagrams of the specific surface free energy determined by the mixture of liquid and solid materials. The equilibrium shape is found by drawing all the planes perpendicular to the radius vector of surface energy and taking the innermost envelop (Fig. 11 (a)). If a faces has a much lower free energy than the other faces, it means that the cusp is sharp and the crystal is faceted. A sharpness of the cusp on the γ plot is related to the roughness of the surfaces at the atomic scale. Fig. 11 (b) indicates a part of the γ plot. Surface A has the lowest surface free energy of γ_A, and surface B is tilted by angle θ and has a surface free energy of γ_B. The distinction between γ_A and γ_B is the energy of the steps on the A surface (Fig. 11 (c)). As a result, a sharp-edged surface has a high step energy and a low step density on a well-developed surface.

The growth form is determined by the faces with the lowest growth rate in each direction (Elwell & Scheel, 1975). The growth rate of each face is determined by the structure of the surface at the atomic scale. Generally, during crystal growth process, liquid phase is adsorbed on the crystal surface, spread on the surface, adhere to the step of the surface, spread along the step, and eventually are combined into the crystal at a kink. When the surface becomes atomically rough, the density of steps and kinks increase, resulting in a high ion integration rate in the crystal, and vice versa. Thus, a well-developed surface has an atomically smooth structure and a low growth rate. The adsorption of the materials dissolved in a solvent or the solvent itself affects the growth rate by changing the surface roughness or filling the growth sites.

The particle shape is affected by the degree of supersaturation. For the most part, the degree of supersaturation affects the growth rate of the other faces. In an environment

with low degree of supersaturation, there is a large difference in growth rate, and there are particles having a specific habit form. If the degree of supersaturation, there are many particles with similar growth rates and rounded shapes of equiaxed crystals.
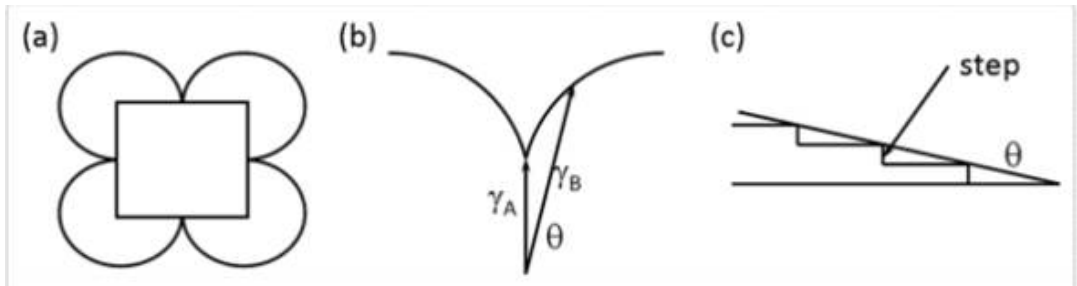
Fig. 12. The equilibrium form is derived from (a) the Wulff plot, (b) the depth of cusp is related to the value of surface free energies (γ_A and γ_B), and (c) the energy of steps on surface A is related to the difference $\gamma_B \to \gamma_A$ [13].

2) Growth shape

a) Rough interface

An interface that is uniquely configured with Kinks is called a "rough interface." Crystal grains reaching such a rough interface can be immediately incorporated into the crystal surface. The growth mechanism of this interface is adhesive type and the interface proceeds uniformly rather than two-dimensionally.
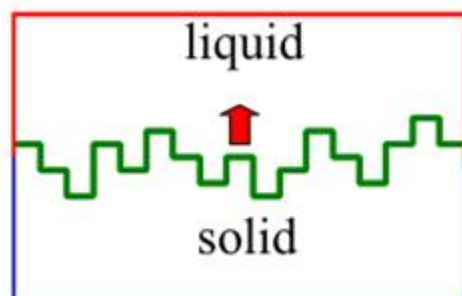
Fig. 13. Scheme of rough interface.

b) Atomically singular interface [14]

Spiral growth and layer growth by two-dimensional nucleation is the growth mechanism of crystals expected to operate on atomically singular interfaces. Terms like "complete plane", "singular plane", and "smooth interface" have been used to denote such an interface.
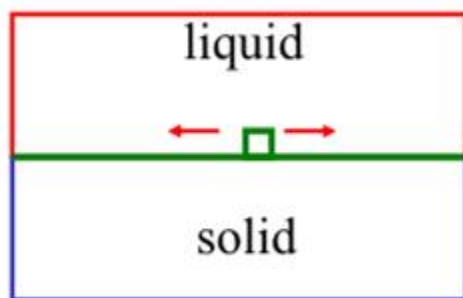
Fig. 14. Scheme of atomically singular
interface.

Depending on the type of interfaces, three types of growth mechanisms, adhesive type, two-dimensional nucleation growth (2DNG) and spiral growth mechanisms are expected. The relation between growths rates versus driving force are different as schematically illustrated in Fig. 14. Therefore, it is understood that the structure of solid-liquid interfaces, rough or smooth, is essentially important in discussing the growth mechanisms and thus forms of crystals.

$$R = A \left(\Delta\mu / kT \right) \qquad R = A \exp \left(-B / \Delta\mu / kT \right) \qquad R = A \left(\Delta\mu / kT \right)^2$$

ROUGH　　　　　　　　　　　SMOOTH
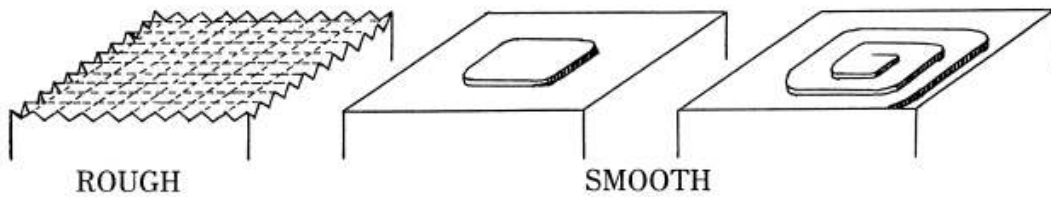
Fig. 15. Interface structures and three types of growth mechanisms R, growth rate; Δμ/kT driving force. (A, B, constants)

3) Kinetics roughening [15]

The physicist Ukichiro Nakaya conducted the first in-depth laboratory research on various types of snow crystals forms in the 1930s. Nakaya classifies natural snow crystals in different meteorological conditions and artificial snow crystals for the first time experimentally in a controlled environment. Nakaya observed various growth patterns in various temperatures and supersaturation, and combined these observations into a snow crystal morphology diagram, shown in Fig. 15. This diagram refers to snow crystals that grows in air at a pressure of about 1 atm, also applies to natural snow crystals. The results of Nakaya have been confirmed and replaced by several subsequent investigations, and the recent data have been extended to low temperatures of T = -70℃. These observations can demonstrate the effect of temperature and supersaturation on crystal morphology. Growth at temperatures near T = -2℃, just below freezing, is similar to plate-like growth. It has a thick plate and a thin plate in each of lower supersaturation and intermediate supersaturation, and a plate-like dendrite structures at higher supersaturation. For temperatures close to T = -5℃, the growth is columnar, with strong columns at the lower supersaturation, frequent slender, often hollow-columns at intermediate supersaturation, and clustered with thin, needle-like crystals at higher supersaturation. It is still colder at around T = -15℃, where growth is again becomes plate-like, and the structure increased as the supersaturation increases again. All of the thin, plate-like crystals grew at temperatures near T = -15℃. Finally, growth at the lowest temperatures becomes a mixture of thick plates at low supersaturation.
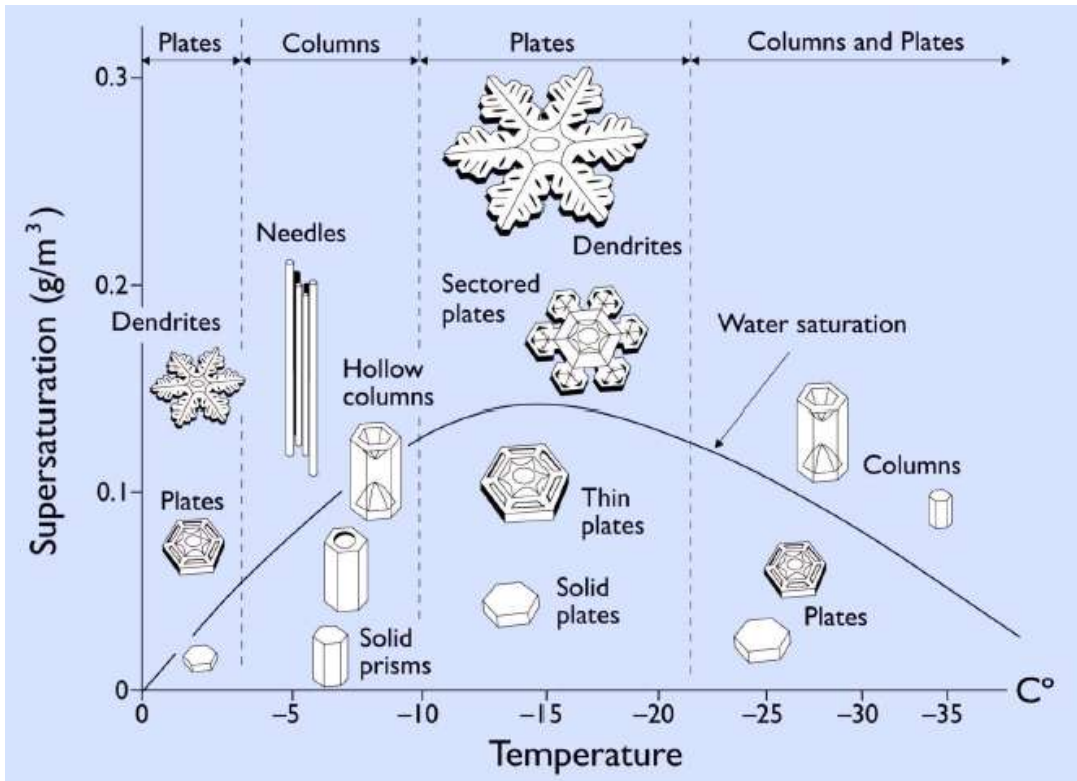
Fig. 16. The snow crystal morphology diagram.

4) Ripening [16]

When providing an overview for the crystal growth kinetics, we should think aabout the influence and power of the Ostwald ripening (OR) mechanism, a classical kinetic model. Early study of the kinetic model for coarsening of crystals was based on the OR mechanism. The OR mechanism means the growth of larger particles at the expense of smaller ones. The driving force for this process is the reduction of total surface free energy.

According to the Gibbs-Thomson equation, the equilibrium solute concentration is lower at the large particles surface than the small particles. As a result, concentration gradients lead to solute ions flowing from small particles to the larger ones. The coarsening mechanism is frequently controlled by the diffusion, particle growth by adding ions to the particle surface from solution. Fig. 16 illustrates the crystal growth via the OR mechanism. The classical kinetic model of the OR mechanism is known as the Lifshitz, Slyozov and Wagner (LSW) models based on the Gibbs-Thomson equation. The general kinetic equation of these cases can be written as:

$$\overline{D}^n - \overline{D}_0^n = \kappa(t - t_0) \qquad \text{eqn (5)}$$

where $\overline{D}$ and $\overline{D}_0$ are the indicate particle sizes at time t and t_0. k is a temperature-dependent material constant, and n is an exponent related to the coarsening mechanism. For example, for n = 3, when it occurs most frequently, the coarsening kinetics are controlled by the volume diffusion of ions in the matrix. From eqn (5), it can be perceived that the growth curve of size versus time fits the parabola, and the crystal size increases continuously with time increasing. The OR mechanism has been widely used to describe and describe the crystal growth of particles with a relatively large size in solution. Experimentalists have confirmed the validity of the LSW theory. The OR growth kinetics are satisfactory, but there is still a small disagreements by experimentally reported particle distributions and OR theory. So, in understanding the OR mechanism, more experimental and theoretical research is needed in this field.
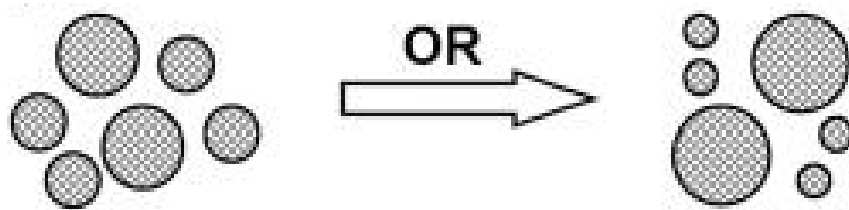
Fig. 17. Scheme of nanocrystal growth controlled by Ostwald ripening mechanism.

5) Abnormal grain growth

In 1996, Park et al. reported the mechanism of the abnormal growth of these faceted WC-Co grains in liquid matrices. The majority of this section is an excerpt from Park's "Abnormal Growth of Faceted (WC) Grains in a (Co) Liquid Matrix" [17].

For example, in the material produced by liquid phase sintering, the shape of the particles dispersed in the liquid matrix is a facet having a substantially spherical or flat plane with a smooth curved surface. Alloys with spherical grains undergo normal Ostwald ripening, while alloys with faceted grains often exhibit abnormal growth.

In metallic systems but also in some oxides and in carbides prepared by liquid-phase sintering, the grains in liquid matrices are nearly spherical if the liquid volume fractions are sufficiently high. The spherical grains represent the equilibrium shape, which in turn implies isotropic interfacial energy. The isotropic surface energy in turn implies an atomically rough surface. Since atom attachment or detachment at the diffusion surface is fast enough to maintain local equilibrium, grain growth is diffusion control and is actually demonstrated experimentally in some of these systems. The spherical grain shape is therefore consistent with diffusion-controlled coarsening. As theoretically predicted, the material systems with spherical grains were found to reach the steady state of an invariant with the normalized size distribution.

In some compound systems, such as WC-Co, TiC-Co, TiC-Co, and HfC-Co and Si_3N_4, $MgAl_2O_4$, and $BaTiO_3$, The grains dispersed in liquid matrices are faceted with flat surface planes. Because these planes are likely to be atomically smooth, the atoms attached to them will be restricted under normal conditions. On the basis of the experimental observations, it has been proposed that the grain coarsening in such systems is controlled by interface reaction. Warren and Waldron [18] observed that when the grains were nearly spherical, and their coarsening behavior agreed with that predicted for the diffusion-controlled mechanism. They observed, on the other hand, that when the grains were faceted with {100} surfaces and their coarsening rates were much lower and the activation energies higher than those measured in spherical grains.

A indication to insight the abnormal growth of the faceted grains can be found in

the growth mechanism of the crystals having a faceted surface planes from the melt or a solution. It was proposed and demonstrated experimentally that the melt and the solution growth of the crystals having a singular planes occurred by defect-promoted mechanisms and by two-dimensional (2-D) surface nucleation. The same mechanisms c be operating in the coarsening of the faceted grains in a liquid matrix and may cause these grains to growth abnormally. The abnormal growth of grains dispersed in a matrix may be defined as the case where the grain size distribution is broader than those predicted by the general Ostwald ripening theories. Although the real size distribution of the grains with complex shapes is difficult to determine, a small fraction of the grains is sometimes observed to be so much larger than the rest that the abnormal growth can be unambiguously identified.

The prediction on the basis of r th that the occurrence of AGG critically depends on the initial grain size was tested on liquid-phase sintered WC-Co using WC powders of 0.85 μm and 5.48 μm in average size. As indicated in Fig. 18, the evolution of the grain structure during sintering of the compacts prepared form this 0.85 μm WC powder at 1500℃. During sintering for 30 minutes, the size of the large abnormal grains increased.
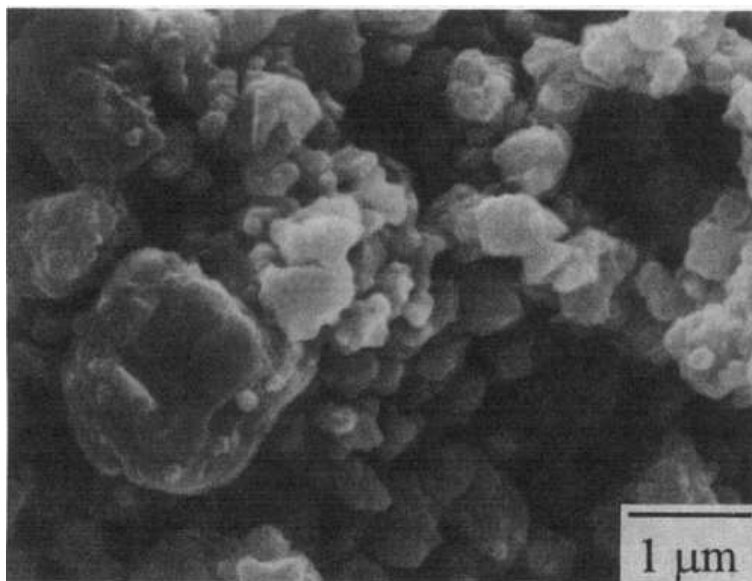
Fig. 18. The scanning electron microstructure of the WC powder of 0.85 ㎛ average size.
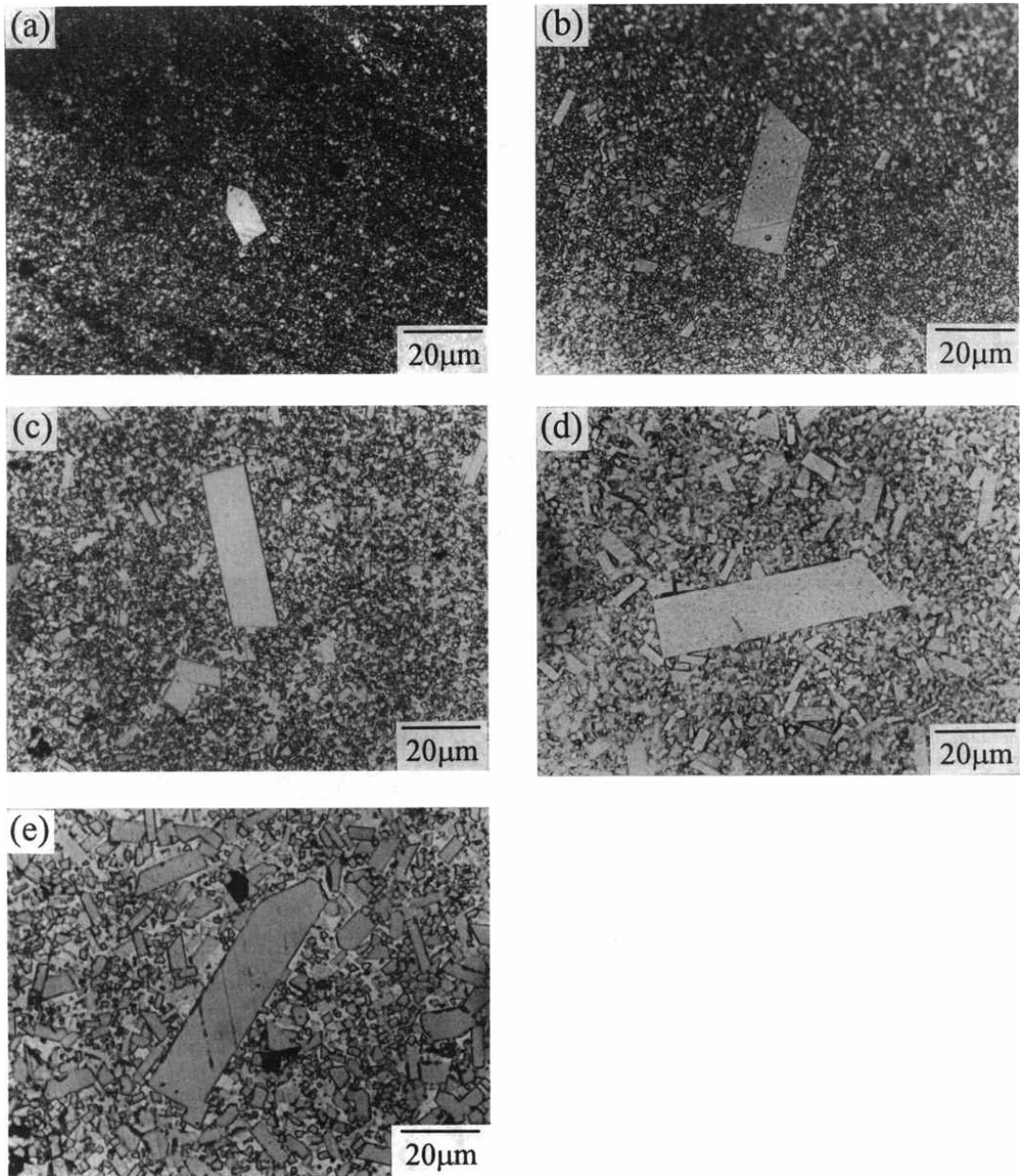
Fig. 19. The microstructures of the WC-15% Co specimens prepared form a 0.85 ㎛ WC powder sintered at 1500℃ for (a) 5 min, (b) 30 min, (c) 1 h, (d) 2 h, and (e) 5 h.

Fig. 19 show the histogram of the grain size distribution for the specimen of Fig. 18 (e). The abnormally large grains had an average diameter of about 35 ㎛, and these had grown from grains about 25 ㎛ in diameter after sintering for 1 hour, as shown Fig. 18 (c). The observed elongated shapes of the large and intermediate size grains appear to represent the cross sections of the truncated flat triangular prisms which have been observed for the extracted grains in this alloy. Their growth is controlled by interface reaction that growth rate is expected to also be anisotropic and may hence influence the shape.
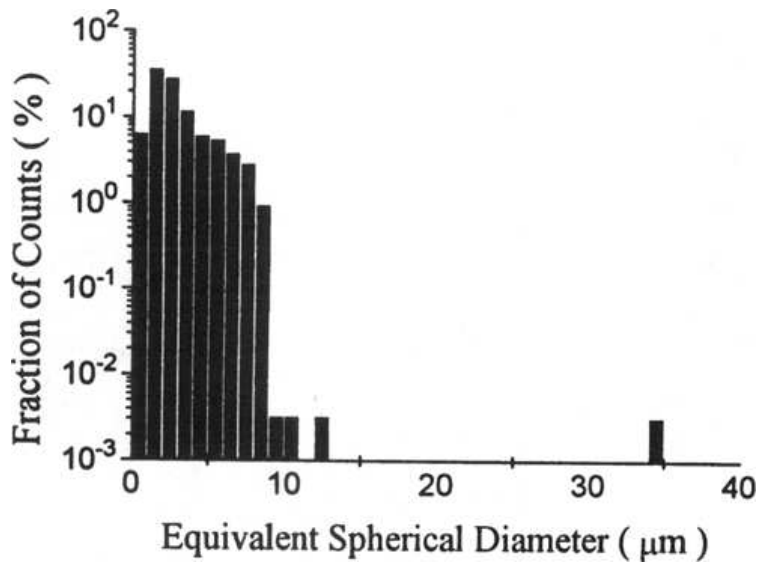
Fig. 20. The grain size distribution in the specimen prepared form 0.85 μm WC.
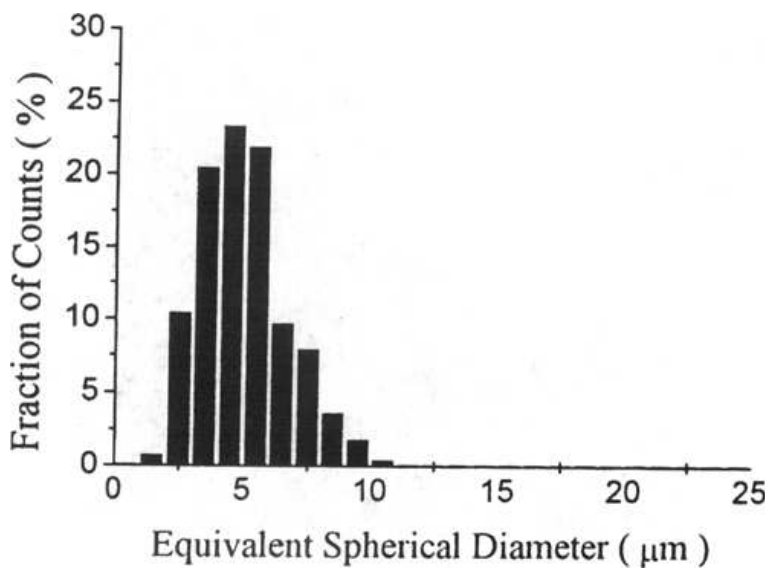
Fig. 21. The grain size distribution of the specimens shown in Fig. 22 (b).

- 37 -

In order to test the prediction that the growth by 2-D nucleation will not occur if the average grain size is larger than the threshold radius r th, the next series of specimens was prepared from a coarse WC powder of 5.48 ㎛ average size. There was almost no change of the grain structure and possibly a slight coarsening, as shown in Fig. 21 (b). The grain size distribution for the specimen sintered for 1/2 hour is shown in Fig. 20 (b) that shows a typical normal size distribution.
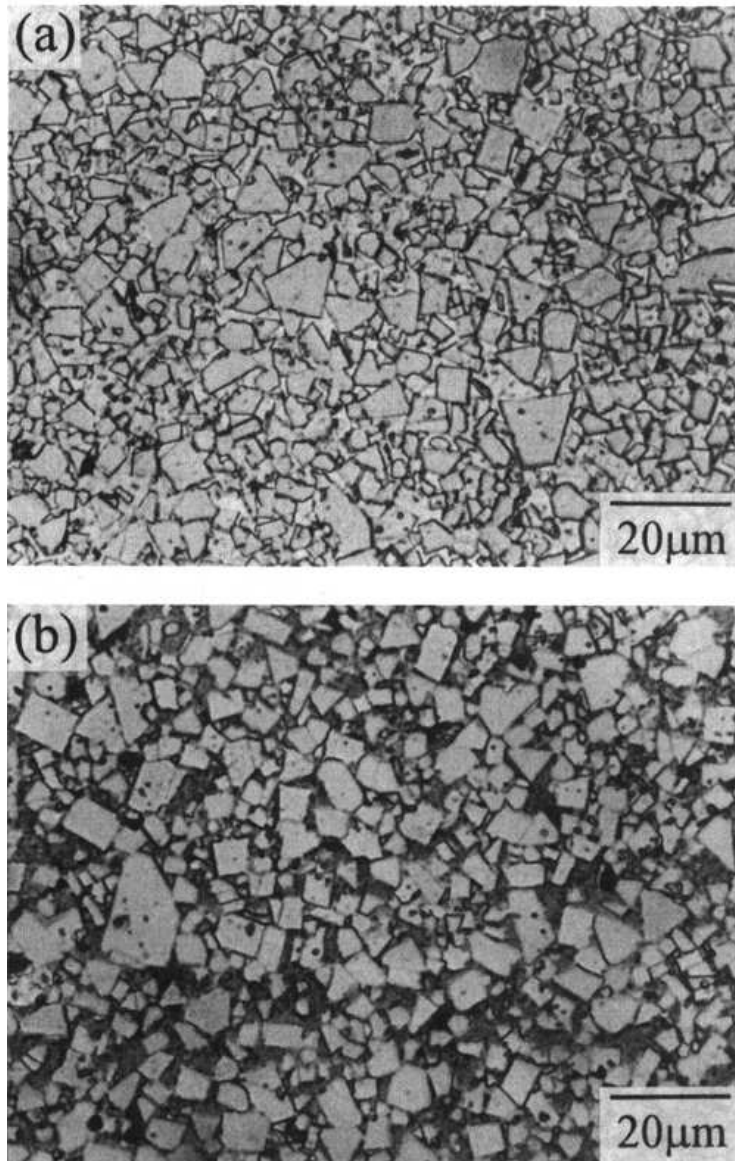
Fig. 22. The microstructures of the specimens prepared from a 5.48 ㎛ WC powder sintered at 1500℃ for (a) 10 min and (b) 20 h.

In the next experimental series, fine (0.85 μm) WC powder was mixed with coarse (5.48 μm) WC powder at the rations of 9/1, 7/3, and 0/10 by weight to test the possibility that the coarse grains grow abnormally if surrounded by fine ones. After sintering for 30 minutes at 1500℃, the specimen of 90% 0.85 μm and 10% 5.48 μm WC powders showed a typical AGG structure, with some grains clearly larger and more elongated than those in the specimens prepared from only 5.48 μm WC powder shown in Fig. 21 (a), 21 (b), and 22 (d) as confirmed by comparing the histograms shown in Fig. 19 and 23. The number density of the abnormally large grains in this specimen was much larger than that in the specimen prepared from only 0.85 μm powder and appeared to be approximately equal to the number density of the 5.48 μm grains.
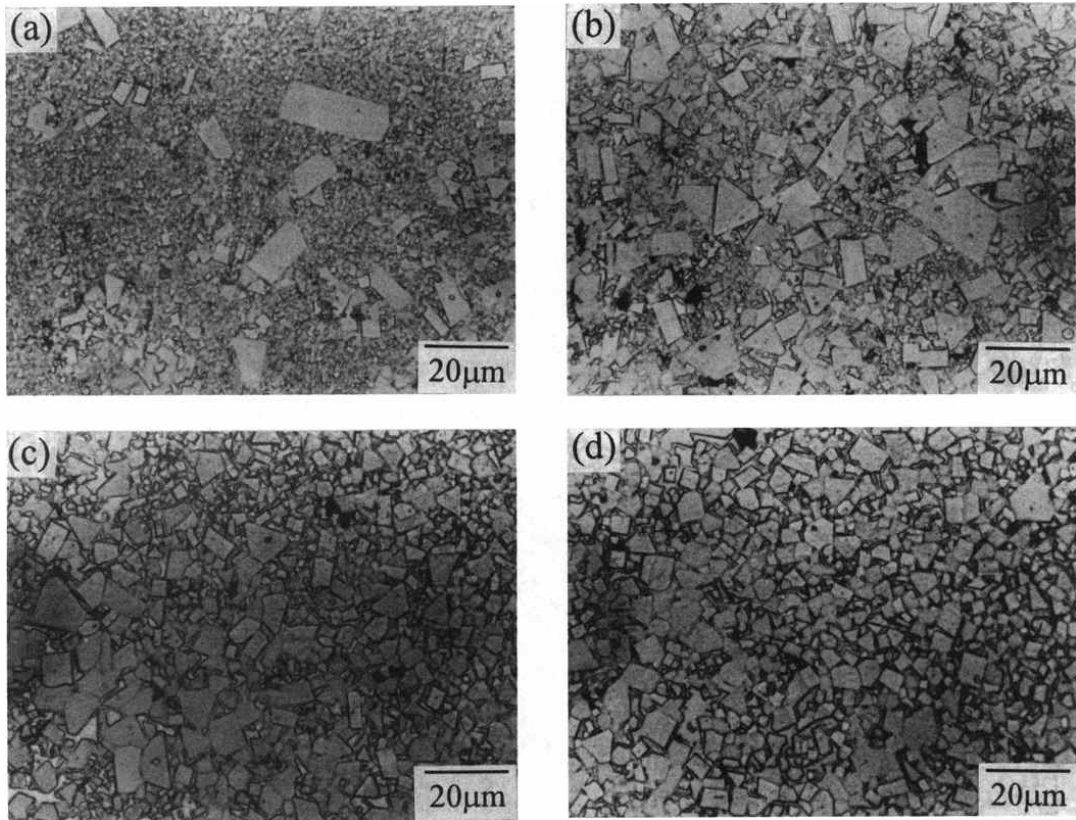
Fig. 23. The microstructures of the specimens prepared from mixtures of fine (0.85 um) WC powders at respective weight percents of (a) 90:10, (b) 70:30, (c) 30:70, and (d) 0:100 and sintered at 1500℃ for 30 min.
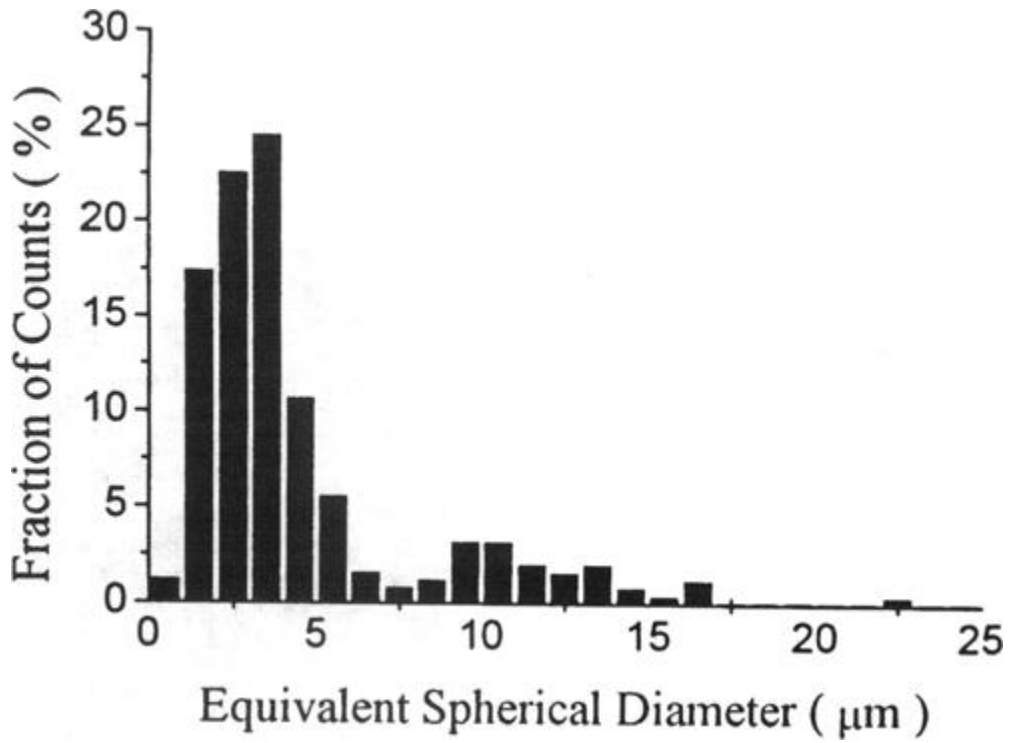
Fig. 24. The grain size distribution of the specimens shown in Fig. 22 (a).

The growth rate of a singular interface that is assisted by 2-D nucleation or defects will increase with temperature as the atomic transfer rate to the surface steps and nucleation energy barrier increases. This prediction was qualitatively confirmed in the specimens prepared from 0.85 ㎛ WC powder and sintered at a higher temperature of 1600℃. As shown in Fig. 24 (a), the specimen sintered at 1600℃ for 5 minutes had a significantly higher number density of the abnormally large grains than those sintered at 1500℃ for 5 or 30 minutes. The observed dependence of the AGG behavior on temperature thus appeared to be consistent with the defect- and 2-D nucleation-assisted growth.
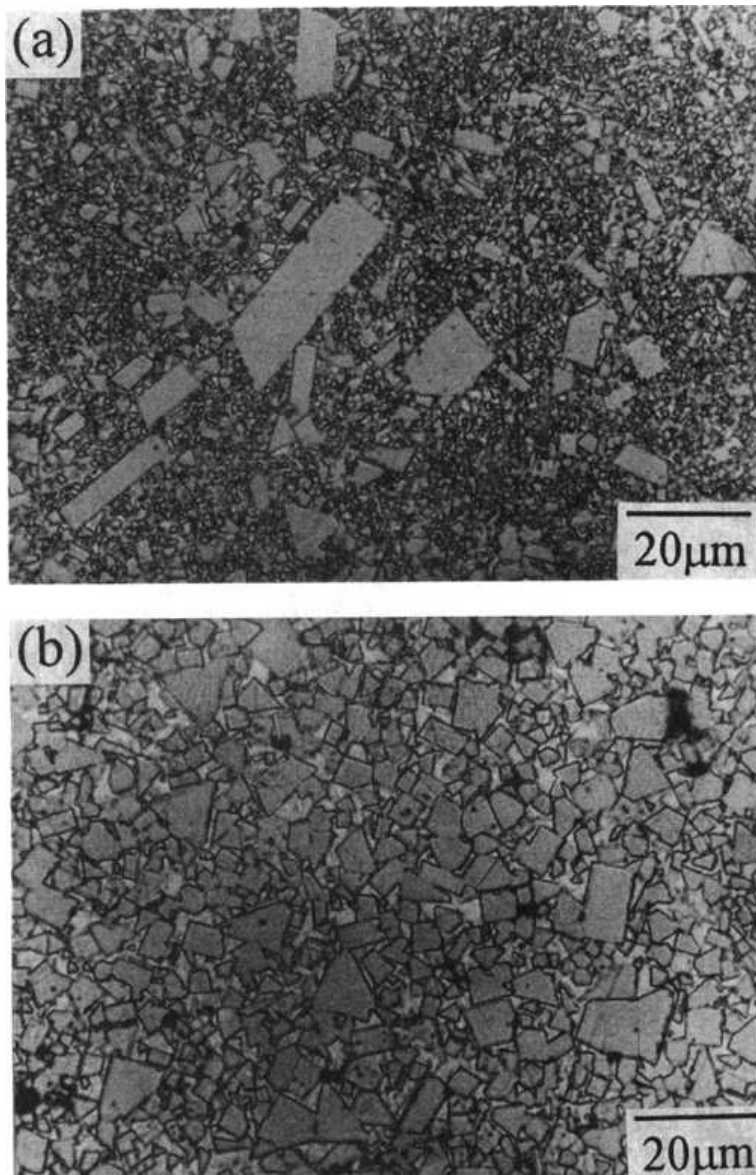
Fig. 25. The microstructures of the specimens (a) prepared from a 0.85 ㎛ WC powder and sintered at 1600℃ for 5 min and (b) prepared from a 5.48 ㎛ WC powder and sintered at 1600℃ for 30 min.

3. Alq$_3$

Fig. 25 shows the structure of the OLED device, which has a emitting layer between a transparent electrode and a metal electrode. To improve the device efficiency, the electron transport layer and the hole transport layer are used above and below the emitting layer, and tris-(8-hydroxy quinoline) aluminum (Alq$_3$) is used most frequently as the material for the electron transport layer and the emitting layer. Therefore, the present study selected Alq$_3$ among the materials used in OLED devices, and the scanning electron microscopy (SEM) measurements of Alq$_3$ powders immediately after synthesis are shown in Fig. 26. It can be observed that Alq$_3$ has irregular shapes with a diameter of approximately 20 ~ 30 ㎛ immediately after synthesis.
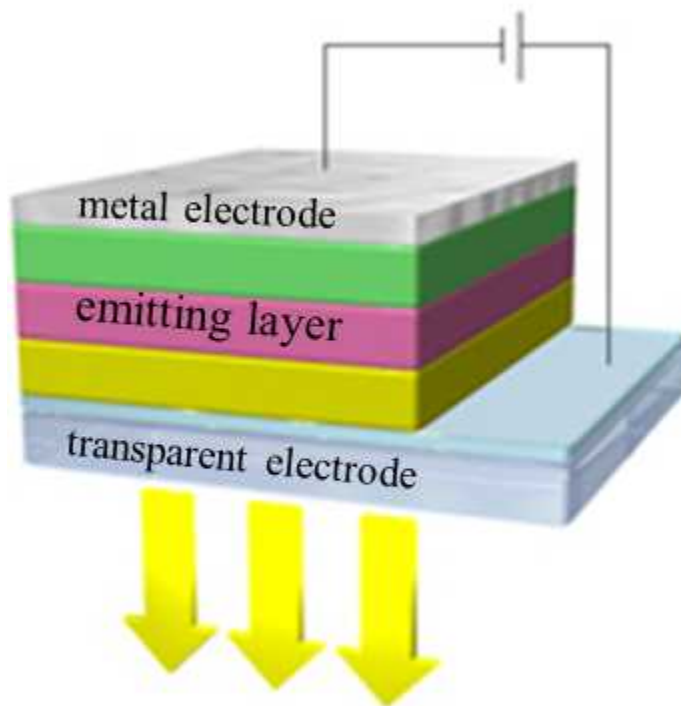
Fig. 26. OLED device structure.
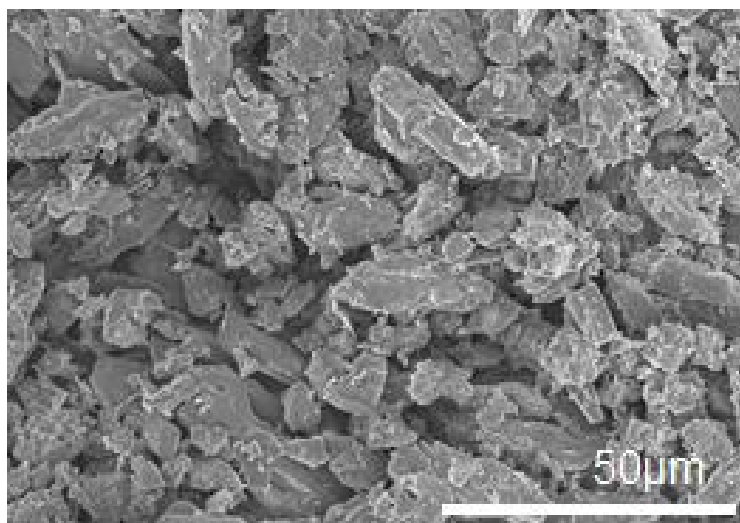
Fig. 27. Alq$_3$ powder after synthesis.

Since Alq$_3$ was first discovered by Tang and Vanslyke in 1987, it has been used in many areas of organic electronic devices, but there search on the electronic and optical properties of Alq$_3$ material, especially its crystalline state, is insufficient [19].

Fig. 27 shows the molecular structure and two isomers of Alq$_3$. The isomer of Alq$_3$ is classified as meridional if the oxygen and nitrogen in the molecular structure form a symmetrical structure, or as facial if they form a mirror structure.

In 2000, the three crystal phases, α-, β-, and γ-phases were first observed by M. Brinkmann et al. [20], in 2002, the δ-phase was first observed by M. Cölle et al. [21], and in 2005, the ε-phase was first observed by M. Rajeswaran et al. [22]. Thus, five Alq$_3$ crystal phases have been reported until now. Fig. 28 shows the X-ray diffraction (XRD) data for the five crystal phases published by M. Rajeswaran et al. [23].

As the molecular structure of organic semiconductor materials is amorphous or polycrystalline, the charge is moved by the hopping system, and hence, the conductivity of the organic semiconductor is low, making it difficult to apply it to actual devices. If charges are moved by the hopping system, the shorter the distance between the molecules, the higher the charge mobility will become; thus, molecular packing will be a crucial factor.

To summarize some studies on the molecular packing of Alq$_3$, M. Cölle et al. observed that δ-Alq$_3$ had an interligand distance of 3.4 Å, which is shorter by approximately 0.5 Å than that of α-Alq$_3$, which was synthesized first and that there was no overlapping part between the ligands of adjacent Alq$_3$ molecules as a result of identifying the crystal structure projected along the c-axis of δ-Alq$_3$ [21]. Furthermore, M. Brinkmann et al. [20] published a paper arguing that, if the orbits of hydroxy quinoline ligands overlap during molecular packing, it would affect the optical characteristics. Based on these findings, it is expected that the conductivity and optical characteristics will be improved if δ-Alq$_3$ with an interligand distance of 3.4 Å, which is shorter than that of other crystal phases, with no overlapping part between ligands is applied to organic semiconductor devices. However, studies on Alq$_3$ until now have reported that it is difficult to obtain pure δ-Alq$_3$ owing to its narrow temperature window.
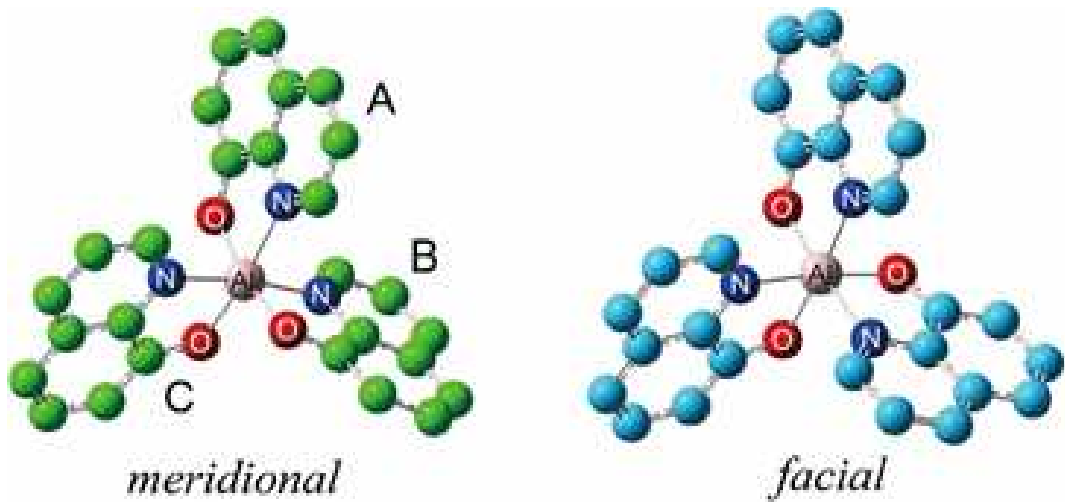
Fig. 28. Two isomeric states of Alq$_3$ [41].
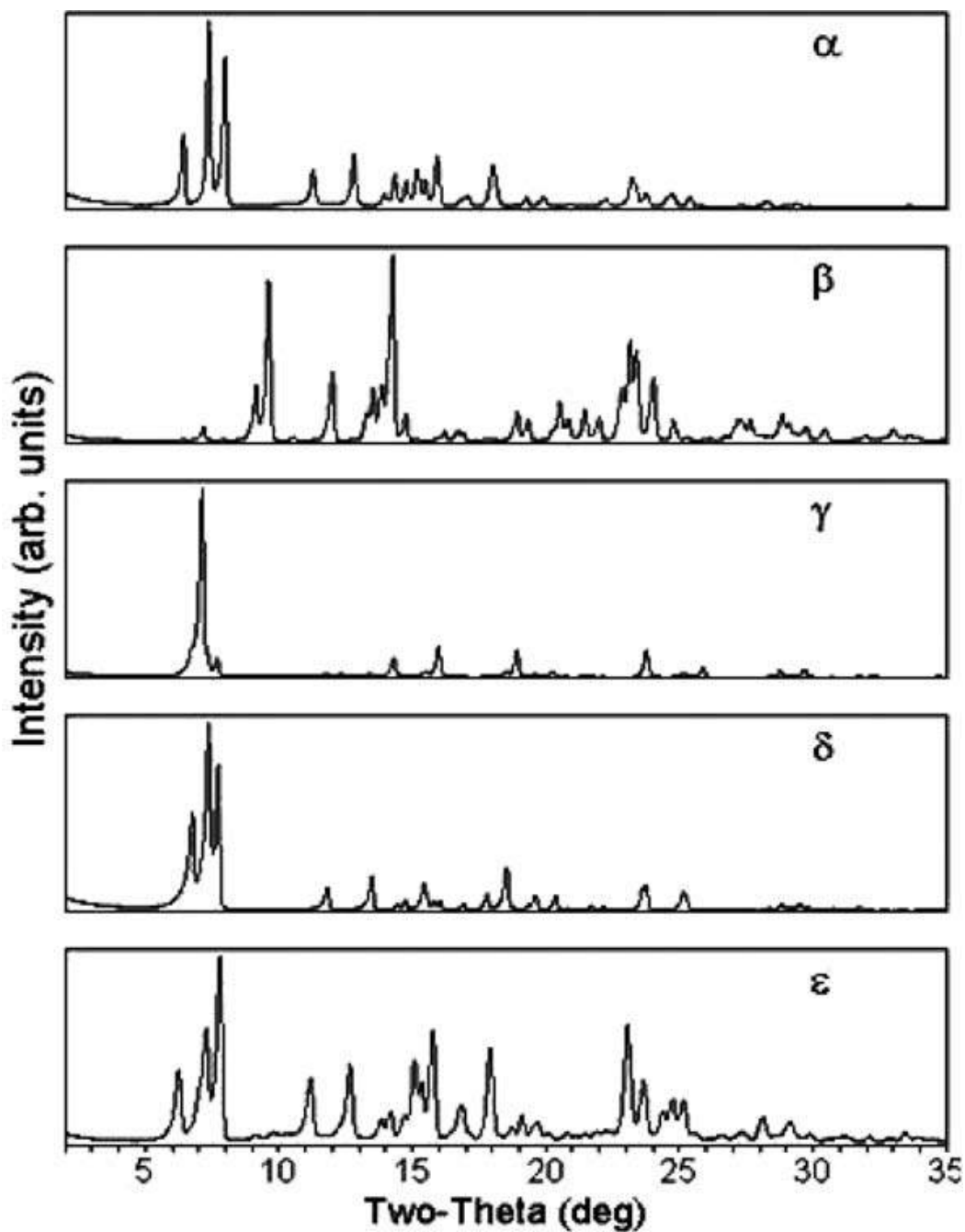
Fig. 29. Room-temperature X-ray powder diffraction patterns for α, β, γ, δ, and ε Alq_3 [23].

- 50 -

4. Ionic liquids

In this study, ionic liquids were used as the solvents for the solution method. Ionic liquids consist of cations and anions and exist as liquid at temperatures below 100℃. They are also called "designer materials" because the structure of cations and anions can be selectively synthesized depending on the purpose of use [24].

Ionic liquids have a low vapor pressure, low volatility, thermal stability, electrochemical stability, and high ionic conductivity. Therefore, they are attracting attention as safe, environmentally friendly solvents to replace conventional solvents such as organic solvents in many industrial fields.

As shown in Fig. 29, ionic liquids are applied to various fields such as solvents for separation process and polymer process, electrolytes of electronic devices such as lithium ion batteries, catalytic reactions of chemical processes, functional liquids, and metal processes. In this study, they were applied to the separation process.

Fig. 30 shows the typical cations of ionic liquids such as imidazolium, tetraalkyl phosphonium, and tetraalkyl ammonium, and many anions such as PF_6^-, $TFSI^-$, Cl^-, and Br^-. In this study, the imidazolium cations and the TFSI anions, which have hydrophobicity, were selected considering the vulnerability of OLED materials to water and oxygen. Furthermore, among the imidazolium cations, the three types of cations - $[C_2mim]$, $[C_8mim]$, and $[C_{12}mim]$ in Fig. 31 - were used in this study.
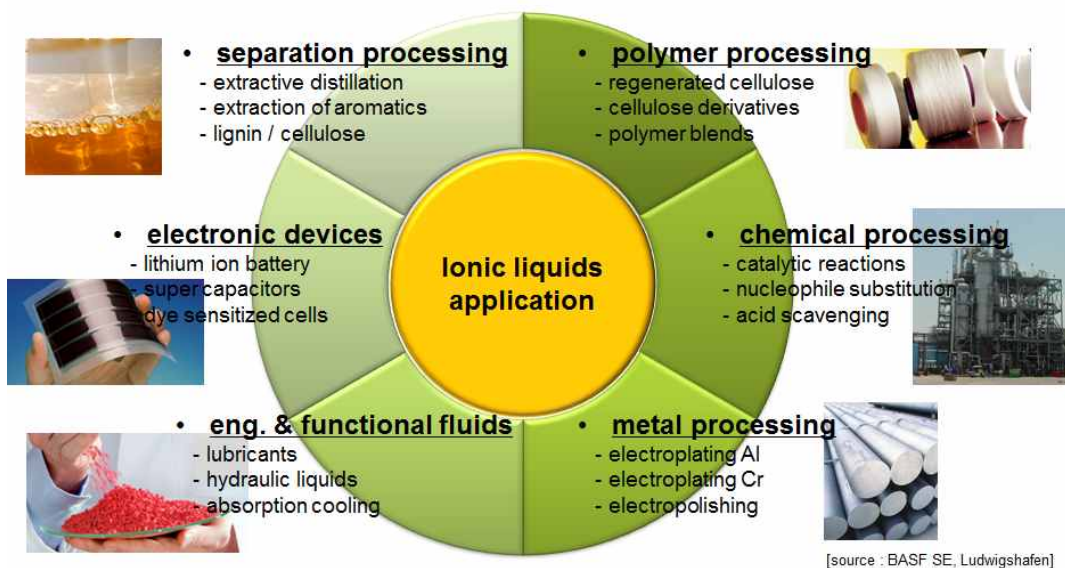
Fig. 30. Applications of ionic liquids.
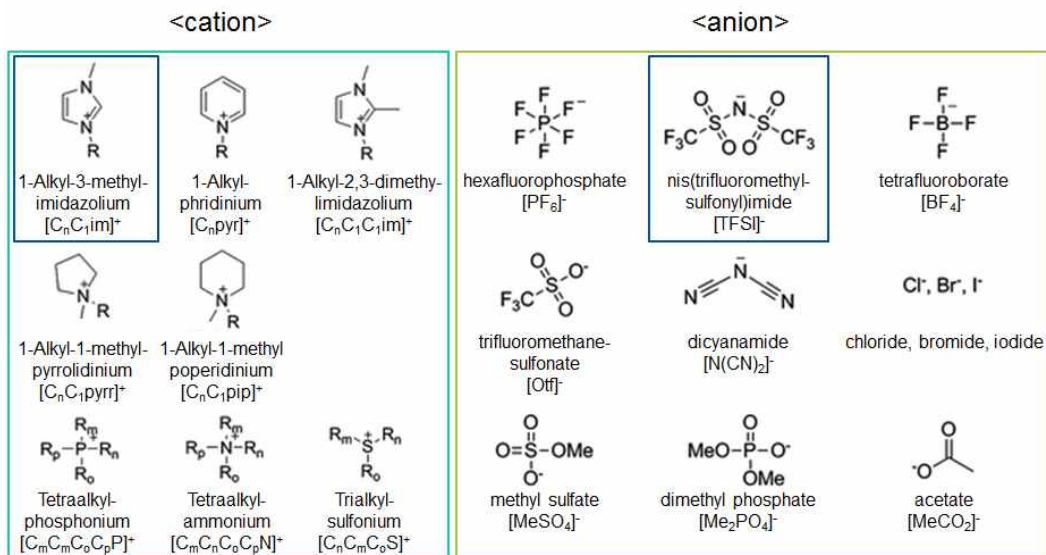
Fig. 31. Typical structures of cations and anions.
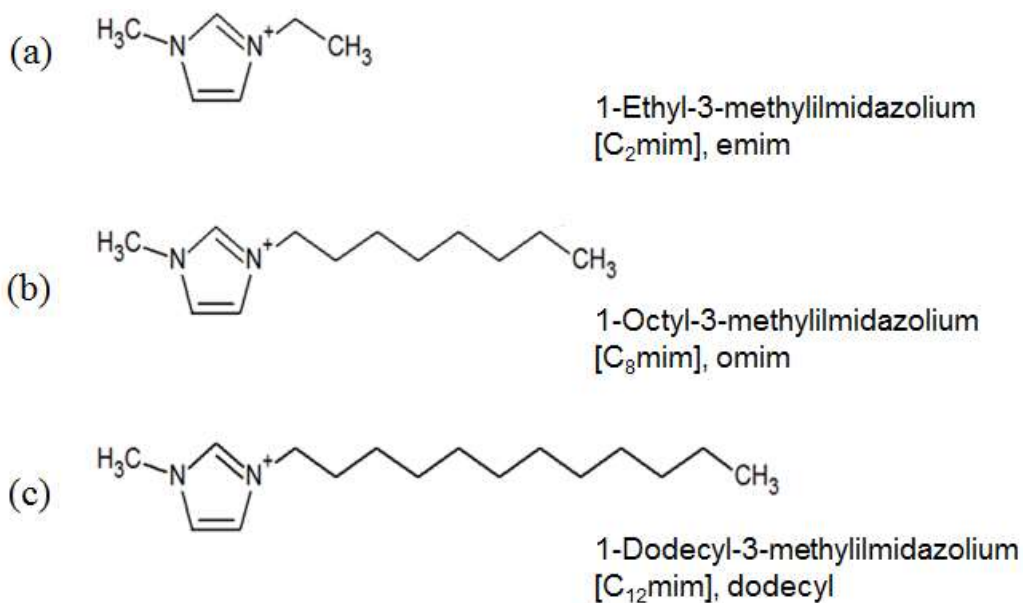
Fig. 32. Cations structure using in this paper (a) $[C_2mim]$, (b) $[C_8mim]$, and (c) $[C_{12}mim]$.

III. EXPERIMENTAL PROCEDURE

In this study, Alq$_3$, which is a representative material used as the emitting layer and electron transport layer in OLED devices, and imidazolium-based ionic liquid were mixed using a magnetic bar for 1 hour. Subsequently, the temperature was raised using a heat-treatment chamber at 5℃/min, and after the heat-treatment according to the predefined experimental conditions, the mixture was quenched. Alq$_3$ and the imidazolium-based ionic liquid were separated and washed with isopropyl alcohol (IPA) and paper filter, and dried in a dryer at 60℃ for over 72 h to obtain Alq$_3$ crystals.

The equipment used in this study is shown in Fig. 32 [11], consisting of a heating plate inside the heat-treatment chamber blocking the external atmosphere. It is designed to allow monitoring of the progress of experiment through a display window and a charge-coupled device camera. The microstructure and shape of the Alq$_3$ crystals were observed using field-emission SEM (FE-SEM, S-4800, HITACHI), and the Alq$_3$ crystal phases were measured at the rate of 0.02 °/s in the range 5 ° ~ 45 ° via the 2θ scan method using high-resolution XRD (HR-XRD, X'PertPROMRD, PANalyticalCo.).
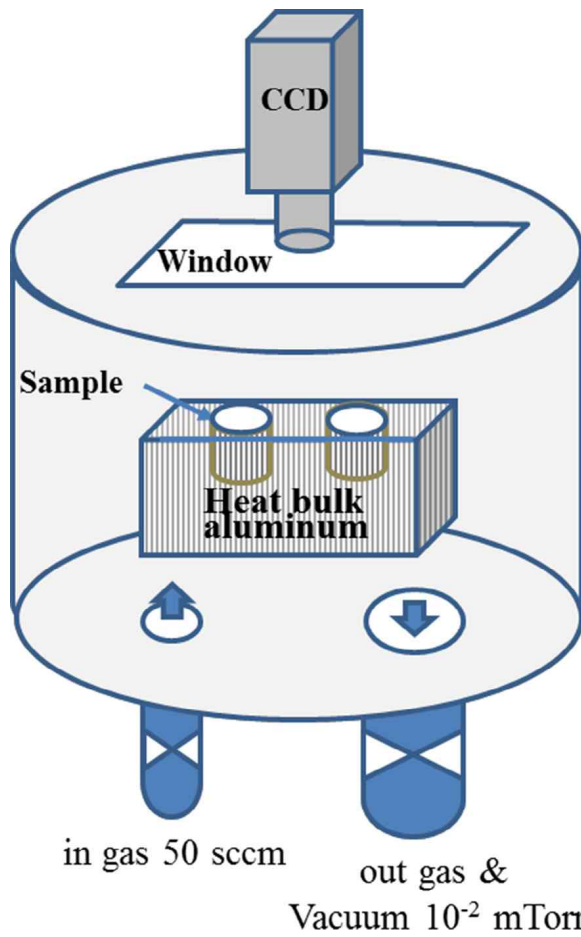
Fig. 33. Schematics of heat-treatment chamber for heat-treatment having heating stage, display window and in-situ CCD camera.

IV. RESEARCH & DISCUSSION

1. Experiment condition

Kim et al. reported a study on the changes of ionic liquids according to the atmosphere and heat-treatment temperature in 2016 [25]. This study confirmed that the descending order of ionic liquids for thermal stability against heat-treatment temperature was [C$_2$mim][TFSI], [C$_{12}$mim][TFSI], and [C$_8$mim][TFSI]. In the case of imidazolium-based ionic liquids, a study observed that, as the alkyl chain length of the cation increases, the ionic symmetry decreases and the Coulombic packing becomes unstable, which lowers the thermal stability [26, 27]. However, as the structural bond between ions is increased by van der Waals force between the hydrocarbons of alkyl chains from 10 or more alkyl chain lengths, the thermal stability of [C$_{12}$mim][TFSI], which has 12 alkyl chains, is higher than that of [C$_8$mim][TFSI], which has 8 alkyl chains. Furthermore, the descending order of stability in the heat-treatment atmosphere was N$_2$, air, and O$_2$. This result suggests that ionic liquids are affected more by temperature than by heat-treatment atmosphere.

As no existing study performed crystal growth of the mixture of ionic liquid and Alq$_3$, the degree of dissolution of ionic liquid and Alq$_3$ was investigated in order to grow Alq$_3$ crystals using an ionic liquid as solvent. Fig. 33 shows the degree of dissolution of the ionic liquid and Alq$_3$ mixed solution, which was mixed using a magnetic bar, at room temperature, observed through an optical microscope. Consequently, [C$_2$mim][TFSI] was dissolved at 0.67 mol%, and [C$_8$mim][TFSI] at 4.1 mol%, but [C$_{12}$mim][TFSI] was not dissolved at room temperature. It can be observed that the alkyl chain length and viscosity of the ionic liquid cations had some effect on the degree of dissolution of ionic liquid and Alq$_3$ at room temperature. The larger the alkyl chain of the imidazolium-based ionic liquid, the greater the viscosity becomes. Thus, if the anion is the same, the viscosity increases when the cation is greater. Referring to published papers, the viscosity of the imidazolium-based ionic liquids at room temperature is 28 ~ 34 cP for [C$_2$mim][TFSI] [28 ~ 32], 47 ~ 69 cP for

[C_4mim][TFSI] [28, 33 ~ 34], and 93 cP [35] for [C_8mim][TFSI]. The viscosity of [C_{12}mim][TFSI] at room temperature has not been reported, but it is estimated to be higher than 100 cP, considering the tendency of increase in viscosity with greater cations, and this appears to be there as on that [C_{12}mim][TFSI] and Alq$_3$ were not dissolved at room temperature.

Fig. 34 shows the degree of dissolution of ionic liquid and Alq$_3$ at the heat-treatment temperature of 100℃ observed with an optical microscope for 3 h considering the future experimental conditions. It can be observed that [C_2mim][TFSI], [C_8mim][TFSI], and [C_{12}mim][TFSI] were dissolved at 1.67 mol%, 6.2 mol%, and 6.8 mol%, respectively. Based on this result, [C_{12}mim][TFSI] was selected as the solvent for the solution method for the growth of Alq$_3$ crystals.
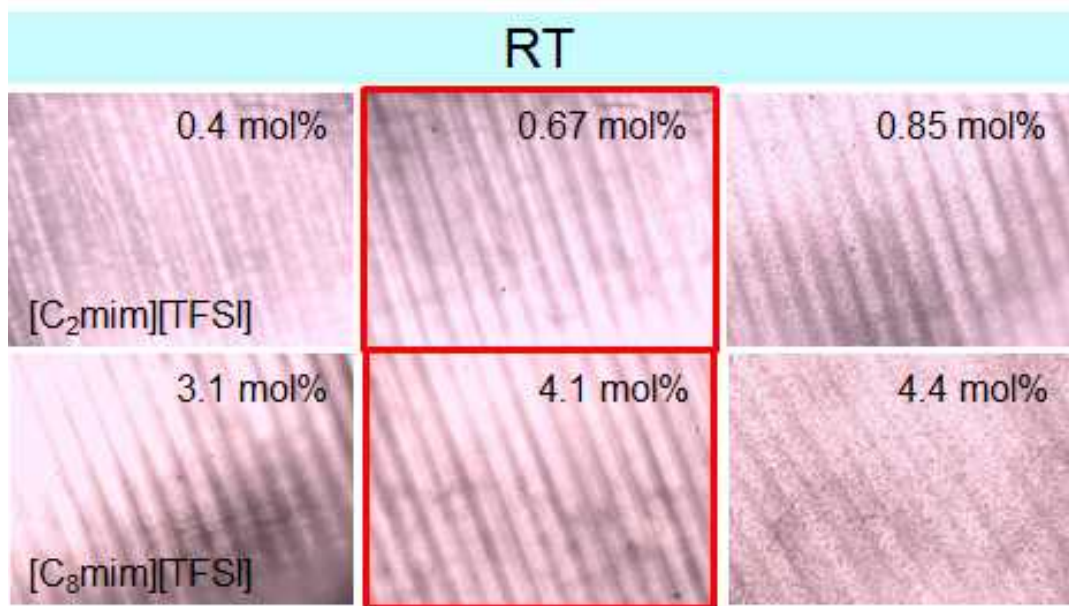
Fig. 34. Optical microscope images confirming the degree of dissolution of Alq$_3$ at room temperature using different ionic liquid cations (a) [C$_2$mim], and (b) [C$_8$mim].
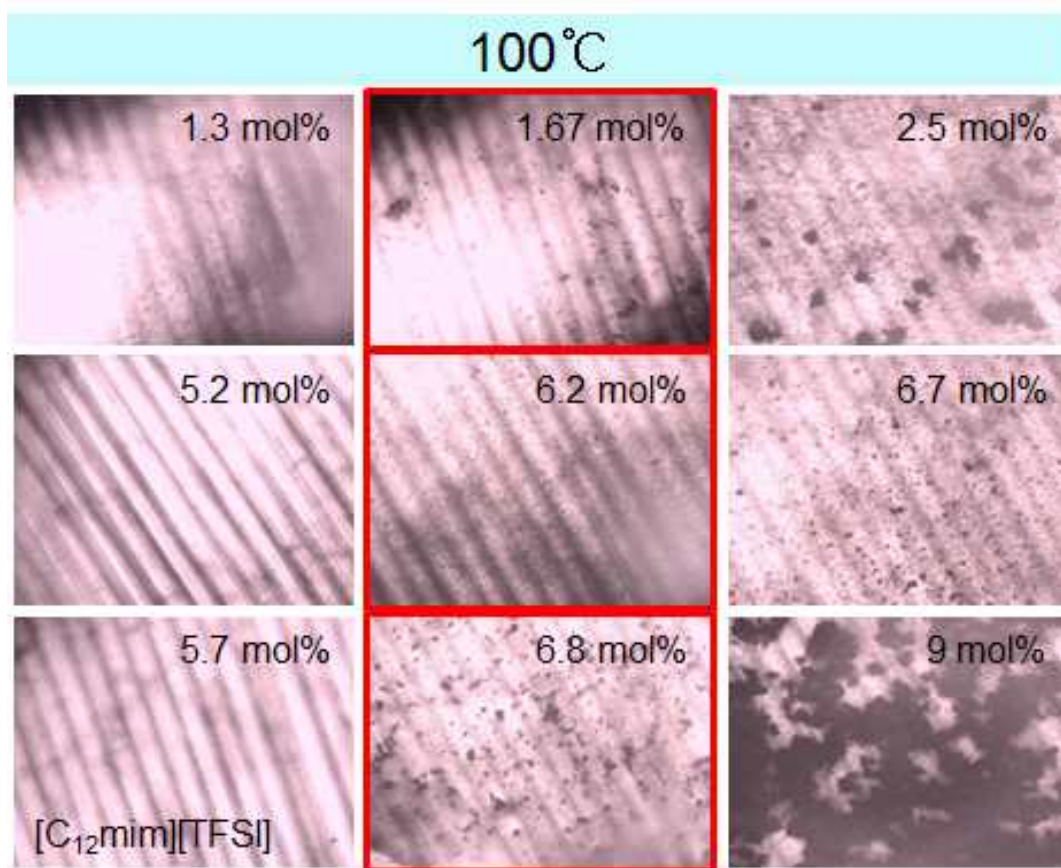
Fig. 35. Optical microscope images confirming the degree of dissolution of Alq₃ at 100℃ for 3 h using different ionic liquid cations (a) [C$_2$mim], (b) [C$_8$mim], and (c) [C$_{12}$mim].

2. Crystal growth depending on the growth temperature and composition

First, a study was conducted to identify the changing tendency of the mixed solution of the [C$_{12}$mim][TFSI] ionic liquid and Alq$_3$ depending on the heat-treatment temperature and composition.

The SEM measurements of the grown Alq$_3$ crystals depending on the heat-treatment temperature and composition are shown in Fig. 35 ~ 40. In general, the Alq$_3$ crystal is close to the growth shape when the heat-treatment temperature is below 120℃. The SEM images show that the hexagonal-rod grows in length along the c-axis and becomes close to the equilibrium shape at heat-treatment temperatures of 160℃ or higher.

Furthermore, the SEM results show that abnormal grain growth occurred under a specific condition. As mentioned above in the theoretical background, abnormal grain growth occurs when the minimum radius at which 2-D nucleation can occur owing to the reciprocal properties is greater than the critical radius, and this condition is influenced by the size of initial nucleation and the degree of supercooling. In this study, abnormal grain growth under a specific condition is shown in Fig. 41. It appeared most distinctly in the specimen of 6 mol% Alq$_3$ that had been heat-treated at 120℃, which can be observed in the SEM image in Fig. 35 (b). Fig. 42 shows the grain size distribution for the condition at which the abnormal grain growth occurred in Fig. 41. The x-axis represents the ratios of the average crystal size and each crystal size, and the y-axis represents the percentage (%) of each ratio in the total. For example, Fig. 42 (a) shows the abnormal grain growth where crystals approximately 3 times larger than the average crystal size constitute approximately 10% of the total. It can be observed that, as this proportion and the heat-treatment temperature increase, they converge to normal grains.

Further, studies that used the solution method to grow Alq$_3$ crystals are examined. J. -S. Hu published a paper on hexagonal-rod shaped Alq$_3$ with a length of approximately 5 ㎛, which was grown via the solution method using a surfactant [10]. W. Chen et al.

produced 1-D Alq_3 nanostructures using a facile solution method and investigated the optical and electrical characteristics of nanowires [36]. The size and shape of Alq_3 can be controlled by the type and concentration of the surfactant. The Alq_3 grown with 60 mg of CTAB (cetyl-trimethylammonium bromide) surfactant grew to a length of 10 μm. W. Xie et al. produced Alq_3 1-D crystals using the volatilization of the solvent at room temperature with no surfactant [37]. The longest Alq_3 1-D crystal was approximately 100 μm, and they claimed that the Alq_3 microrod can be controlled by the growth environment such a the concentration of the Alq_3 solution or the volatilization speed of the solvent. Furthermore, rice-like nanoparticles were produced when the concentration of the Alq_3 solution was insufficient. This was mainly because the concentration of the Alq_3 solution has a direct effect on the growing time of Alq_3 crystals and the difference in the growing times of Alq_3 nuclei affects the differences in the grain shape and size.

According to the studies published so far, the maximum length of Alq_3 crystals grown using the solution method is approximately 100 μm. Ref. 10 measured the field emission of Alq_3 crystals of size 100 μm or more and the turn-on field was lower than that of organic or inorganic nanomaterials and similar to that of organic charge-transfer complex nanowires. From this result, it is expected that crystalline Alq_3 with a large grain size can improve the characteristics of organic electronic devices. However, the existing solution methods have many problems in mass production because they use highly toxic surfactants or employ the volatilization of solvent for crystal growth. The solution method used in this study is different from the existing methods because it does not use surfactants and the ionic liquid, which is the solvent, is environmentally friendly.

Fig. 36. SEM images of 6 mol% Alq$_3$ crystal heat-treated at different growth
temperature (a) 100℃, (b) 120℃ (c) 140℃, (d) 160℃, and (e) 180℃.

Fig. 37. SEM images of 8 mol% Alq$_3$ crystal heat-treated at different growth
temperature (a) 100℃, (b) 120℃ (c) 140℃, (d) 160℃, and (e) 180℃.

Fig. 38. SEM images of 10 mol% Alq$_3$ crystal heat-treated at different growth
temperature (a) 100℃, (b) 120℃ (c) 140℃, (d) 160℃, and (e) 180℃.

Fig. 39. SEM images of 12 mol% Alq$_3$ crystal heat-treated at different growth temperature (a) 100℃, (b) 120℃ (c) 140℃, (d) 160℃, and (e) 180℃.
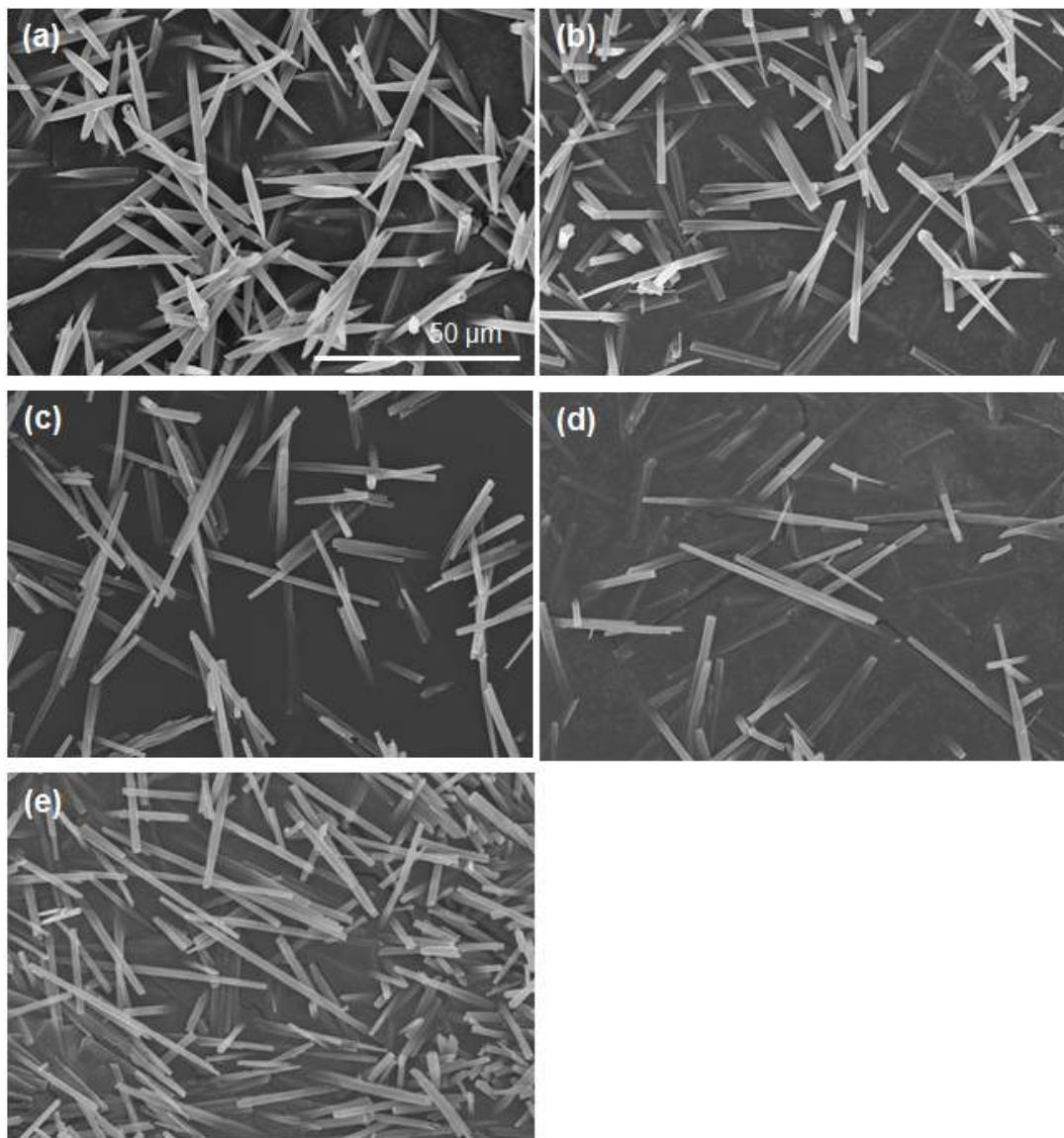
Fig. 40. SEM images of 14 mol% Alq$_3$ crystal heat-treated at different growth temperature (a) 100℃, (b) 120℃ (c) 140℃, (d) 160℃, and (e) 180℃.
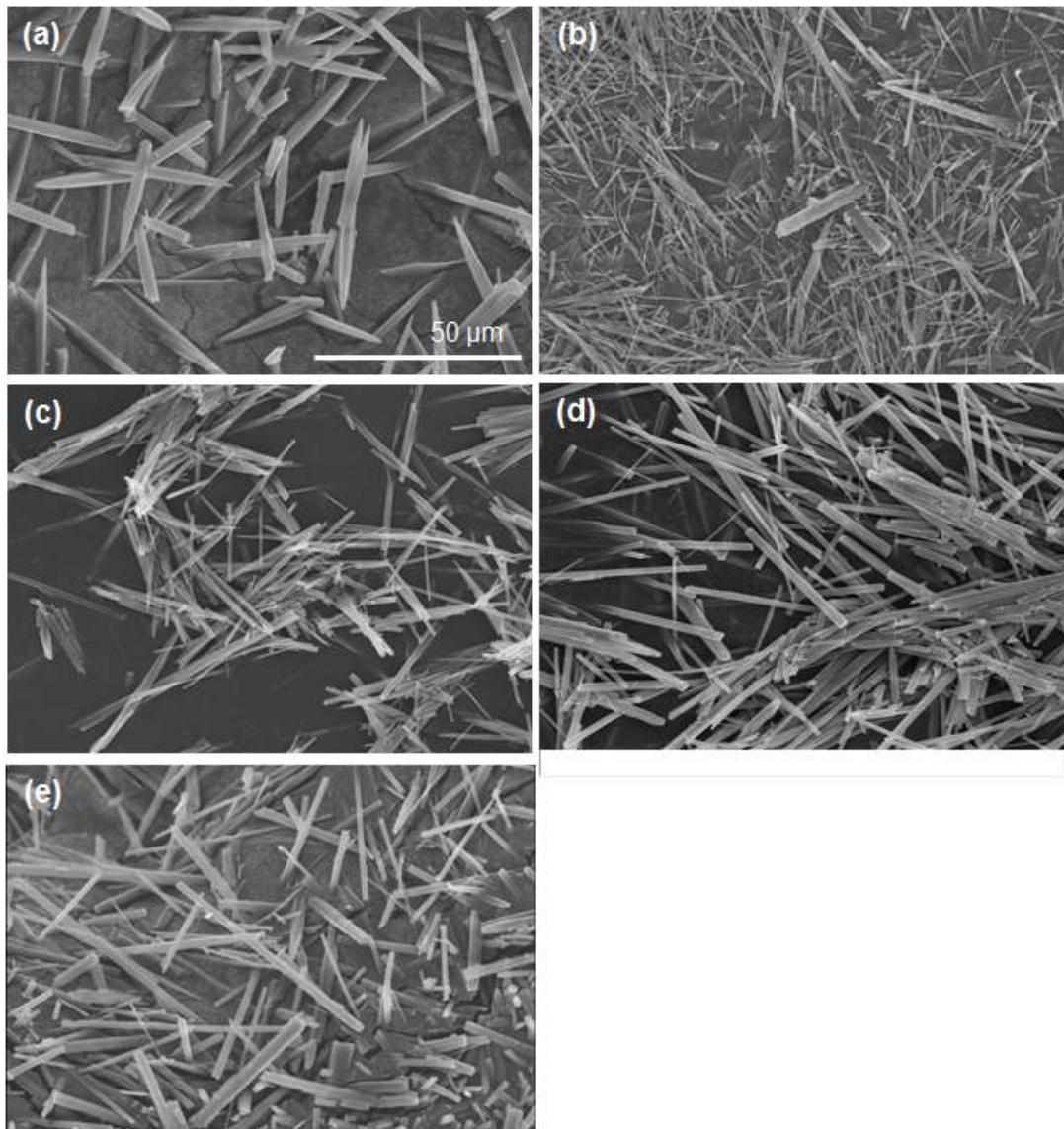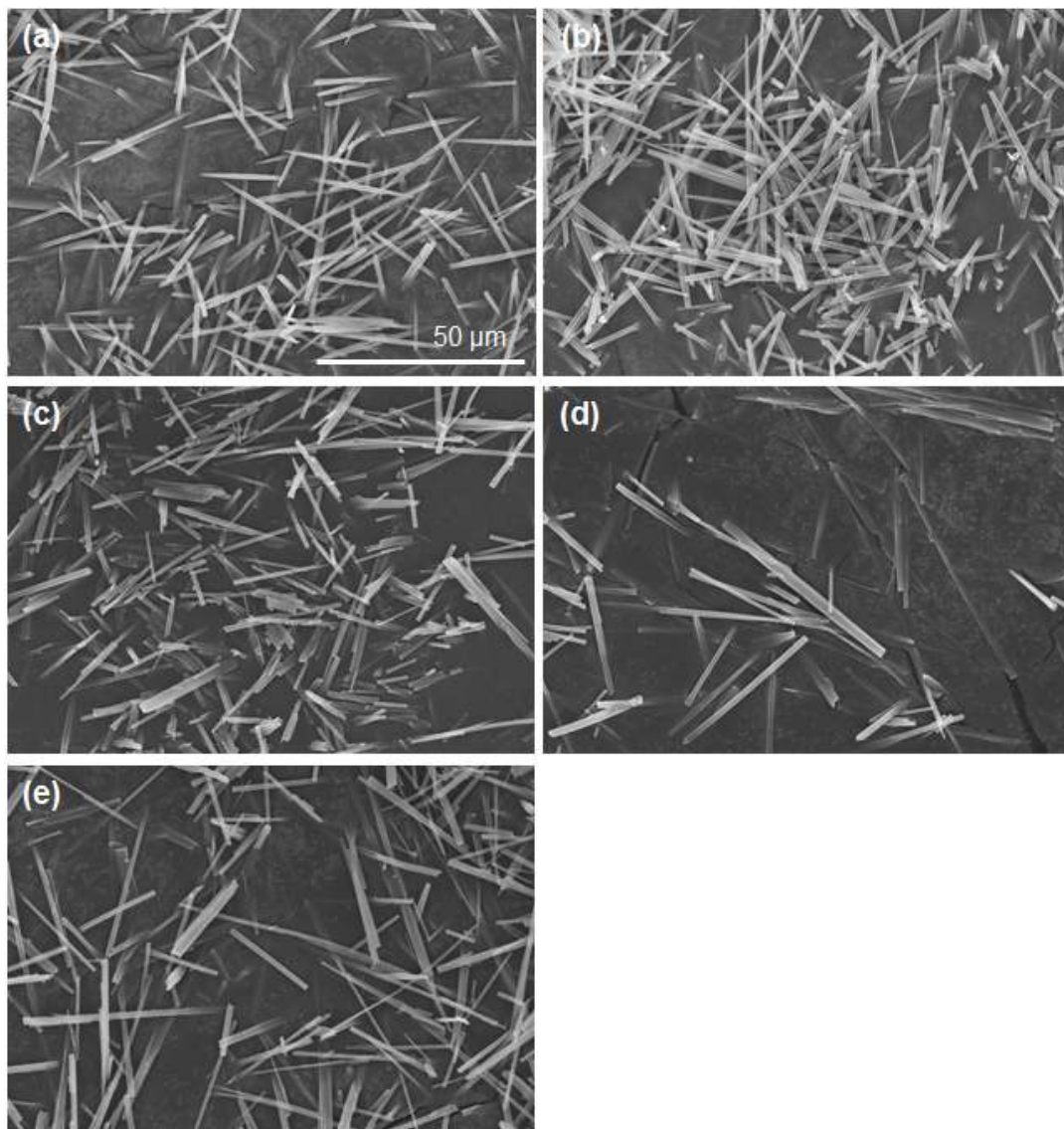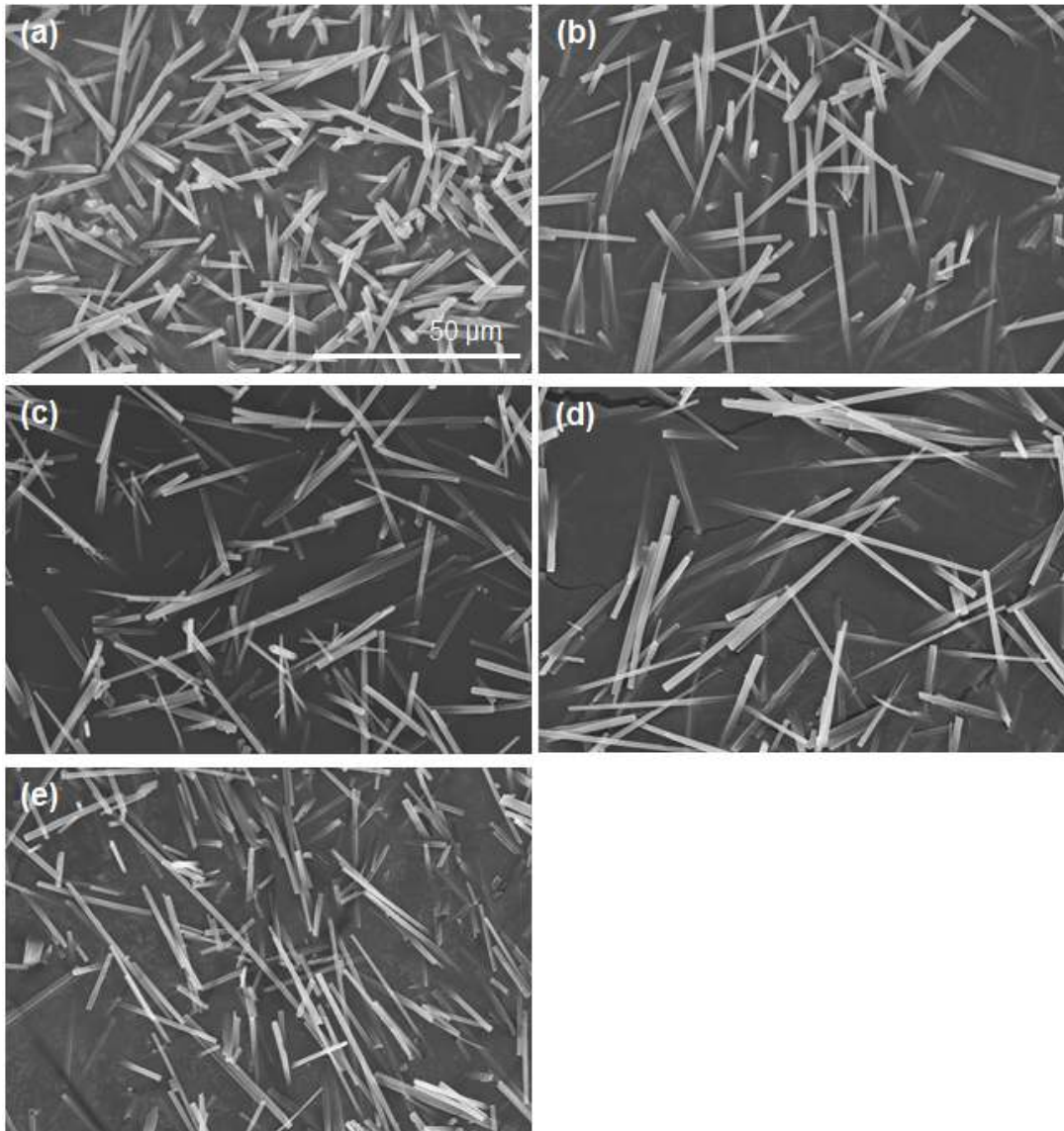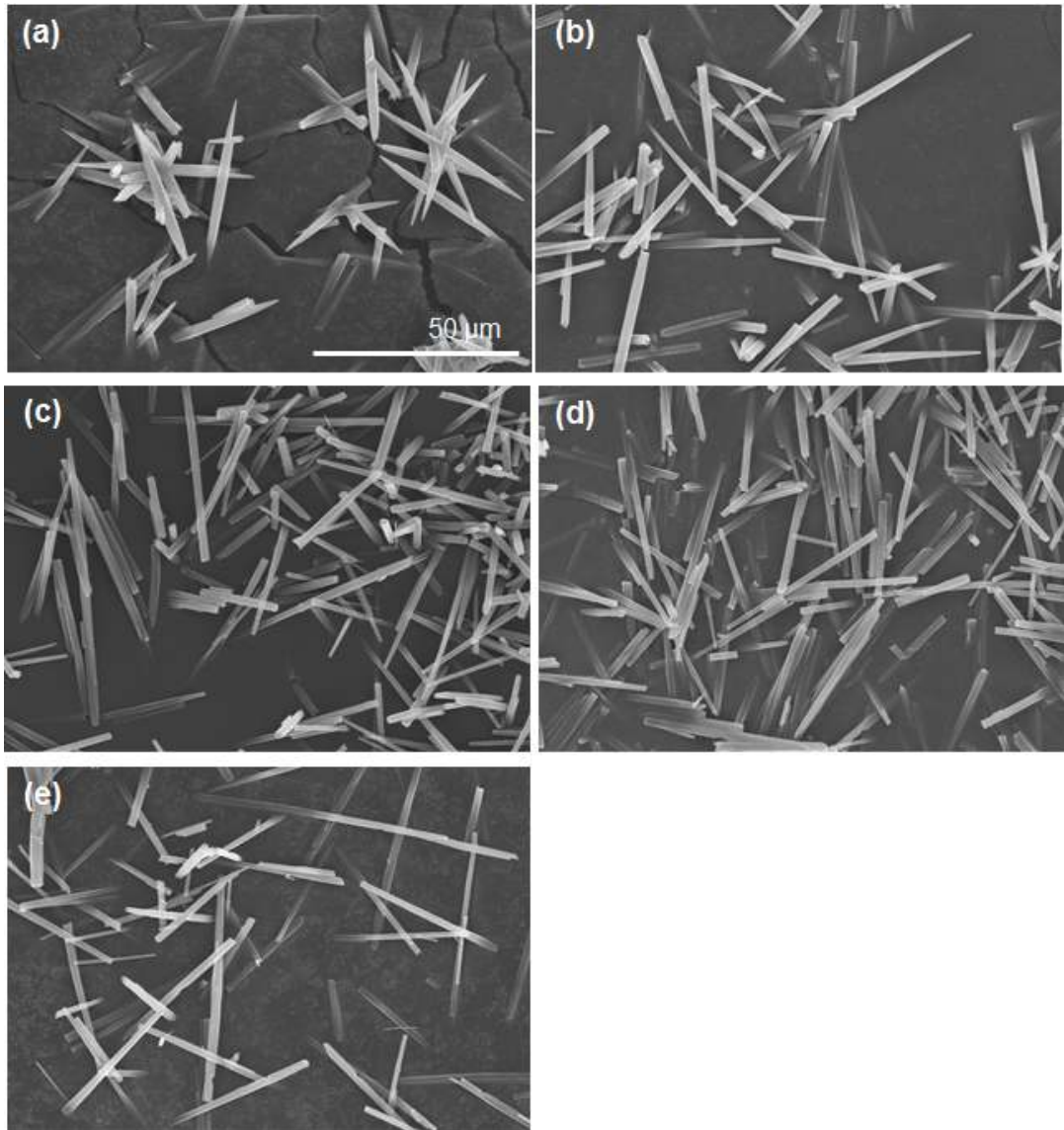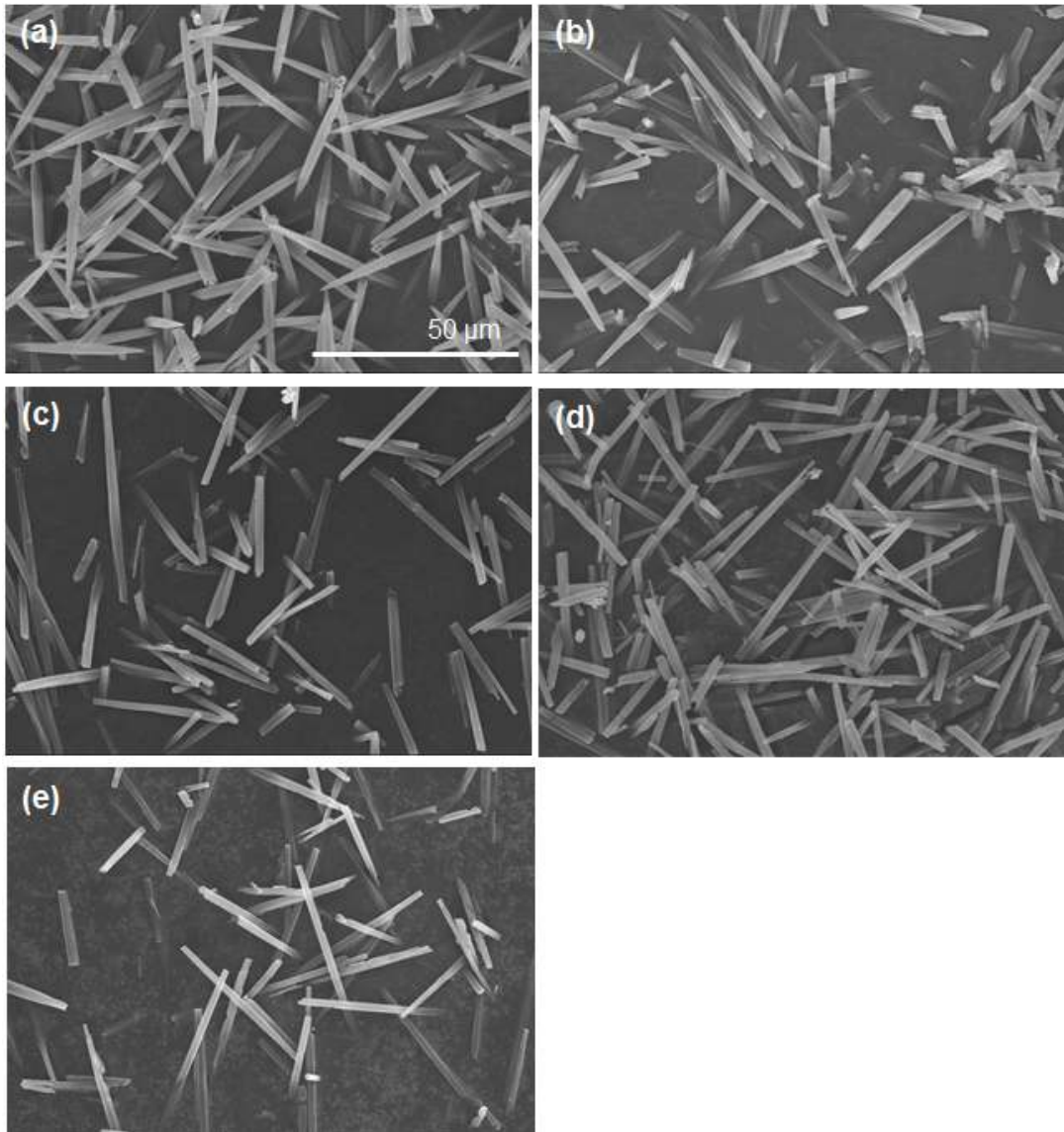
Fig. 41. SEM images of 16 mol% Alq$_3$ crystal heat-treated at different growth temperature (a) 100℃, (b) 120℃ (c) 140℃, (d) 160℃, and (e) 180℃.
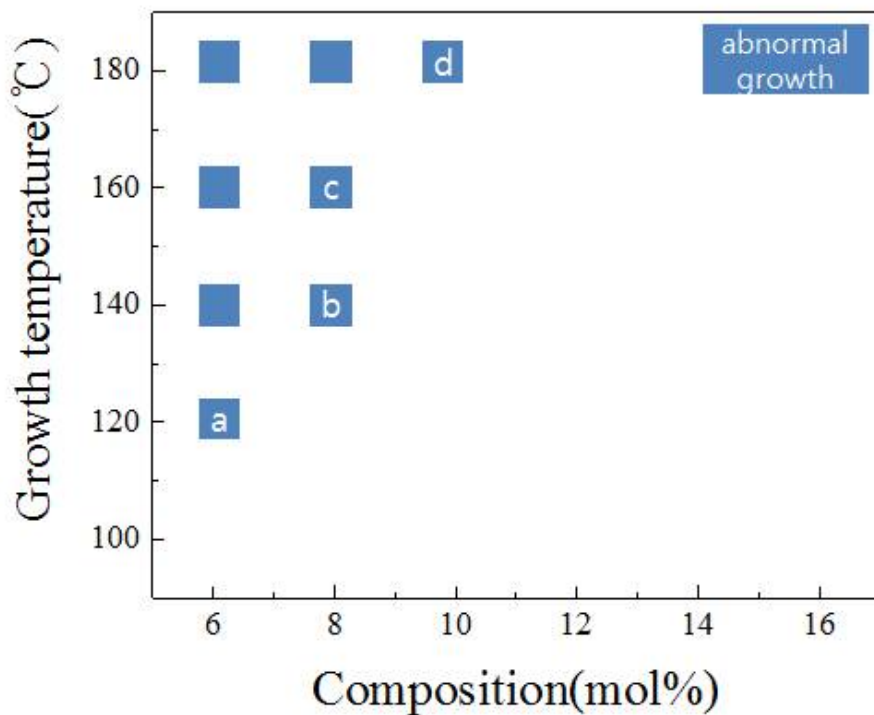
Fig. 42. A summary of the observed variation of the Alq$_3$ crystal growth behavior with compositions & growth temperature.
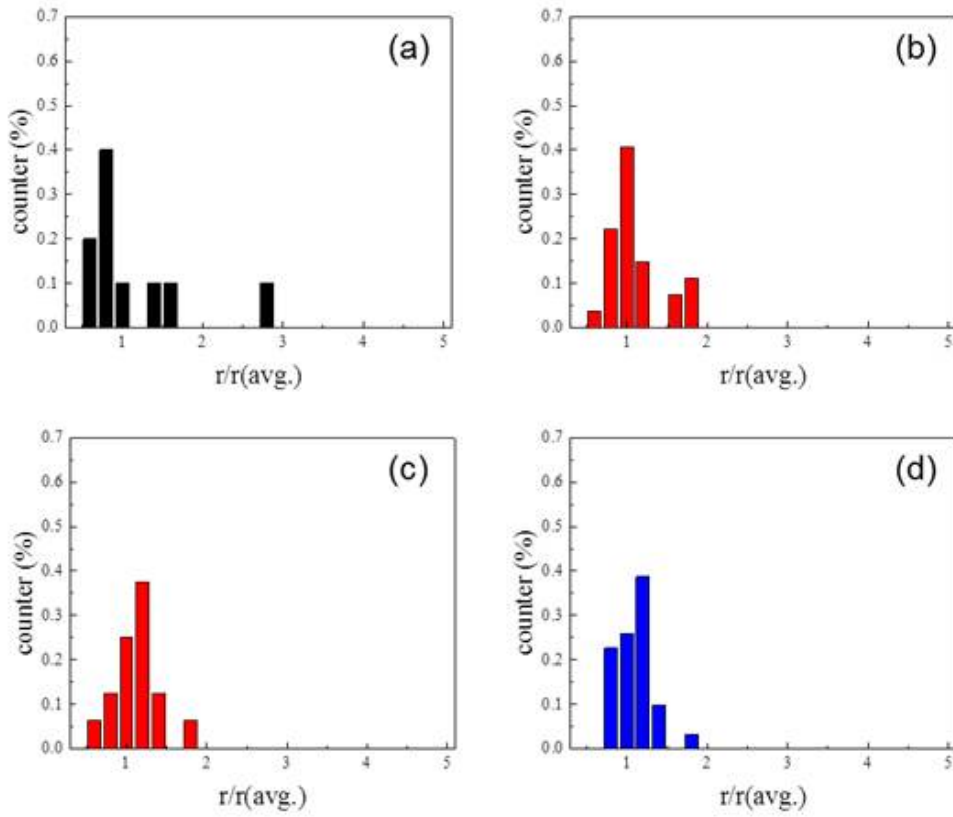
Fig. 43. The measured Alq$_3$ crystal length distribution of the specimen shown in Fig. 41 (a) ~ (d).

The studies related to Alq$_3$ crystal phases published so far are outlined below. α-Alq$_3$ powder scan be obtained via heat-treatment at 400℃ for 2 h and they emit yellowish-green fluorescence [38]. The XRD peaks show $(0\bar{1}2)$, $(1\bar{2}1)$, $(0\bar{2}3)$, and $(\bar{1}12)$ planes at the 2θ positions of 12.4 °, 18.7 °, 20.0 °, and 21.1 °, respectively [23]. β-Alq$_3$ crystals can be easily obtained by the sublimation of β-Alq$_3$ powders in a tube furnace at 280℃ and the crystal phases have triclinic crystals [23]. Dark yellow substances were obtained after heat-treatment of Alq$_3$ powders for several minutes at a high temperature of 410℃ and were verified as γ-Alq$_3$ via XRD measurement. In addition, new peaks that had not been observed in the XRD of existing crystal phases were observed at the 2θ positions of 7.05 ° and 25.85 ° [38]. F. H. Kao et al. reported an XRD peak on the (001) plane of γ-Alq$_3$ at 7.05 ° [39]. M. Cölle et al. obtained δ-Alq$_3$ via heat-treatment of α-Alq$_3$ at 390℃ for 6 h and published the XRD data analysis results of δ-Alq$_3$ [21, 38, 40].

M. Rajeswaran et al. obtained ϵ-Alq$_3$ via the heat-treatment of β-Alq$_3$ at 350℃ for 5 min and reported that, compared with α-Alq$_3$, the XRD diffraction pattern of ϵ-Alq$_3$ showed a significant difference in the 2θ range 9 ° ~ 11 ° [22]. In some of the results of these previous studies, the analyses of the Alq$_3$ crystal parameters do not match, and hence, only the data about α-Alq$_3$ is registered on the JCPDS card. Thus, more in-depth research on the phase changes for the isomers of Alq$_3$ is necessary. Excluding the controversial results of published papers related to XRD analysis, the XRD measurement results were analyzed in this study based on the papers on the common analysis of Alq$_3$ crystal phases [38, 41].

The XRD measurement results of Alq$_3$ specimens depending on heat-treatment temperature and composition are shown in Fig. 43. When crystal was grown at the composition of 8 mol% and the heat-treatment temperature of 100℃, and at the composition of 16 mol% and the heat-treatment temperature of 100℃, β-Alq$_3$ remained, which is the initial powder phase of Alq$_3$, and as the heat-treatment temperature increased, γ-phase, γ + δ-phase, and pure δ-Alq$_3$ were observed. It was reported in an existing study that it was difficult to obtain pure δ-Alq$_3$ because it has a narrow temperature window. However, pure δ-Alq$_3$ for which the peak that appears in γ-phase

was not detected could be obtained via crystal growth using an ionic liquid at the composition of 16 mol% and the heat-treatment temperature of 180℃.
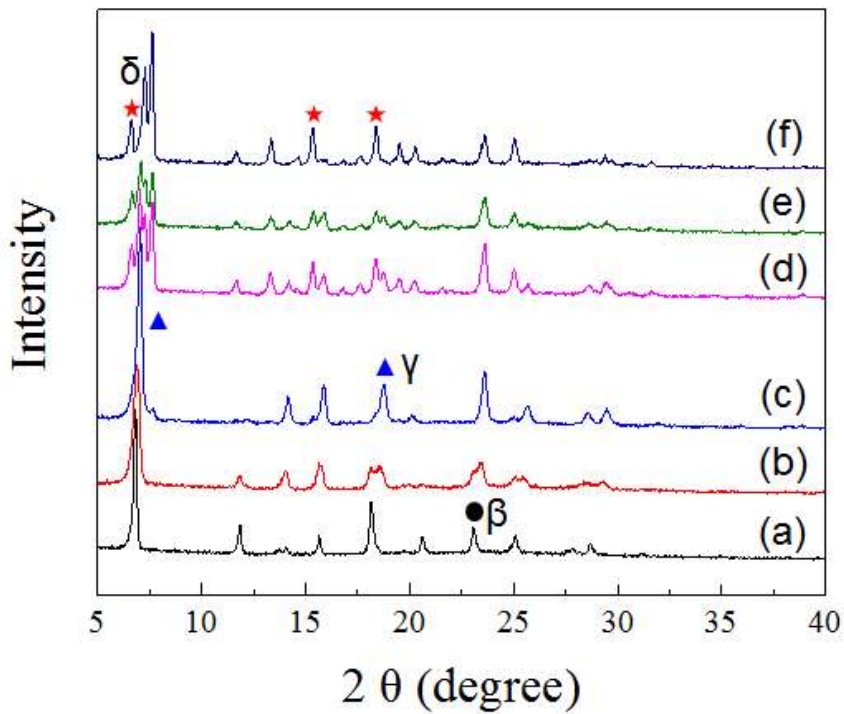
Fig. 44. XRD data of the Alq$_3$ crystal grown at different compositions & growth temperature (a) 8 mol%, 100℃, (b) 16 mol%, 100℃ (c) 16 mol%, 120℃, (d) 16 mol%, 140℃, (e) 16 mol%, 160℃, and (f) 16 mol%, 180℃.

Figs. 44 and 45 show graphs comparing the length and diameter of Alq_3 crystals obtained under each condition. These data are based on the SEM measurements of Alq_3 crystals at low magnification (500×). The results showed a tendency of length growth as the heat-treatment temperature increased in the case of low compositions - 6 mol%, 8 mol%, and 10 mol% Alq_3. In the case of high compositions - 12 mol%, 14 mol%, and 16 mol% Alq_3 - the grain size decreased owing to significant initial nucleation and short nucleation time. Thus, the growth mechanism of Alq_3 crystals via the solution method in [$C_{12}mim$][TFSI] was investigated.
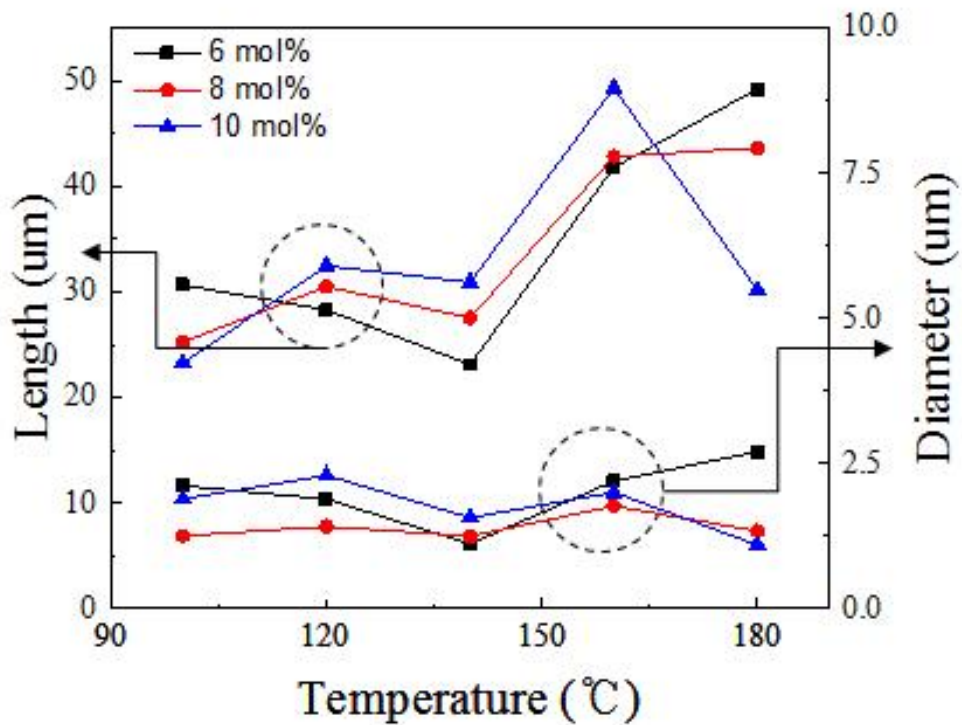
Fig. 45. Length and diameter data depending on the isothermal heat-treatment temperature for 6 mol%, 8 mol%, and 10 mol% Alq$_3$ crystals.
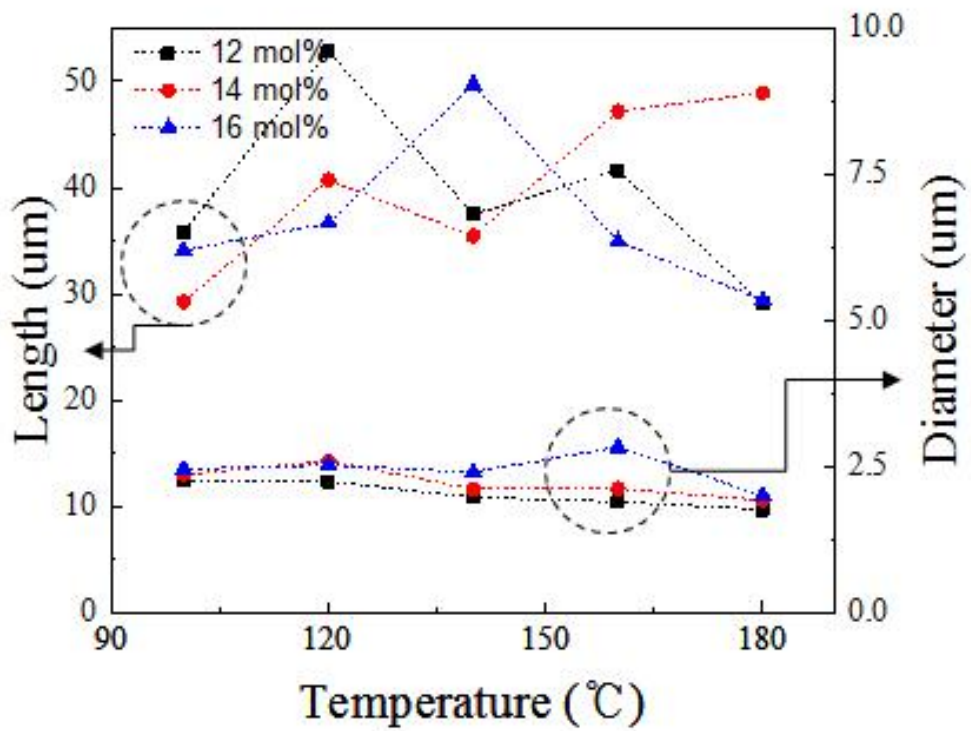
Fig. 46. Length and diameter data depending on the isothermal heat-treatment temperature for 12 mol%, 14 mol%, and 16 mol% Alq$_3$ crystals.

3. Growth mechanism of Alq$_3$ crystals in the [C$_{12}$mim][TFSI] ionic liquid

The growth mechanism of Alq$_3$ crystals in the [C$_{12}$mim][TFSI] ionic liquid was investigated based on the results of Alq$_3$ crystal growth depending on the changes of heat-treatment temperature and composition.

Fig. 46 shows the FE-SEM observation results of the crystal growth pattern according to the isothermal heat-treatment time after the [C$_{12}$mim][TFSI] ionic liquid and 9 mol% Alq$_3$ were mixed and dissolved at 100℃. Figs. 46 (a) and (b) show the Alq$_3$ crystals obtained via isothermal heat-treatment for 1 h and 3 h, respectively. They grew to the shape of a hollow hexagonal-rod with a rough surface and irregular cross-section, and irregular crystals with the size of 20 ~ 30 ㎛ were formed. Figs. 46 (c) and (d) show the Alq$_3$ crystals obtained via isothermal heat-treatment for 24 h and 120 h, respectively. They grew to the shape of a solid uniform hexagonal-rod with a smooth surface, gentle tip of the crystal growth surface, an average length of 30 ㎛, and a hexahedral cross-section. These results confirm that the Alq$_3$ crystals grown in the [C$_{12}$mim][TFSI] ionic liquid at 100℃ grow to the shape of a hollow hexagonal-rod at first and there after to the shape of a solid hexagonal-rod as the isothermal heat-treatment time increases.
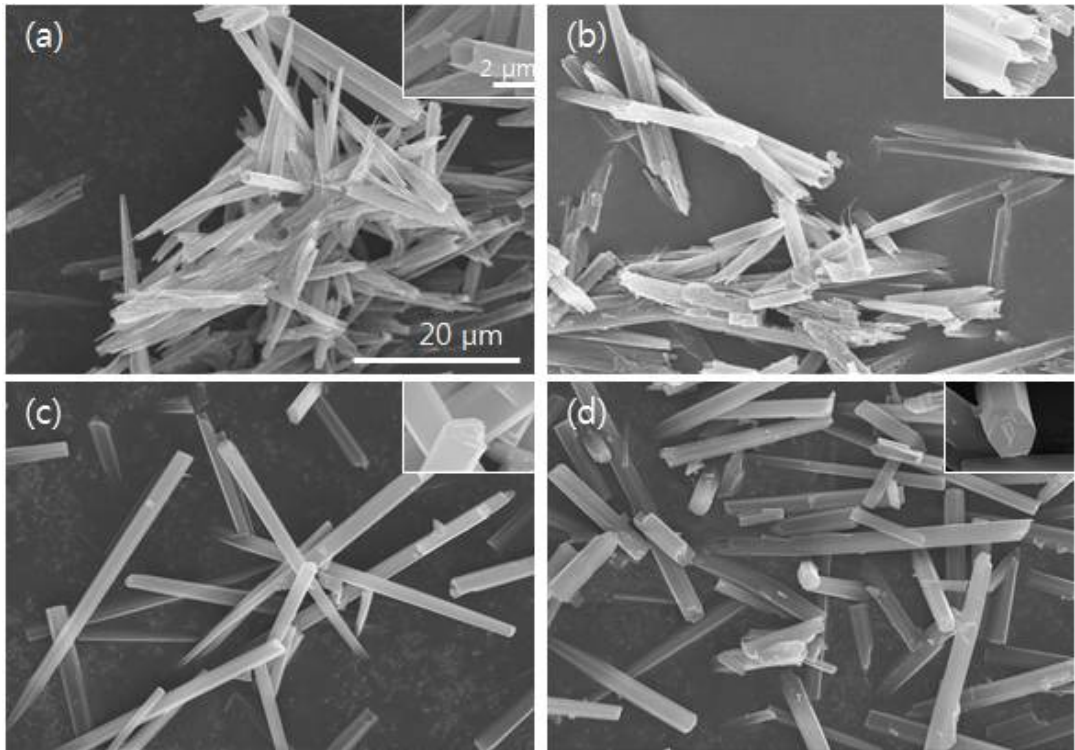
Fig. 47. SEM images of 9 mol% Alq$_3$ crystals obtained over time at the isothermal heat-treatment temperature of 100℃ (a) 1 h, (b) 3 h, (c) 24 h, and (d) 120 h.

Fig. 47 shows the results of HR-XRD measurement conducted to investigate the crystal structure of the specimens in Fig. 46. Before the isothermal heat-treatment, the Alq$_3$ powder contained a mixture of α- and β-Alq$_3$. However, in the case of the specimen for which isothermal heat-treatment was performed in an ionic liquid, some crystal phases of Alq$_3$ immediately after synthesis remained in the early stage of isothermal heat-treatment, and as the isothermal heat-treatment time increased, γ-Alq$_3$ crystal phases were observed. Fig. 47 (c) shows the (001) plane of γ-Alq$_3$ at the 2θ of 7.006 °. Furthermore, when the isothermal heat-treatment time was 120 h, the peaks in the δ-Alq$_3$ crystal phases were observed at 6.667 °, 7.308 °, and 7.601 °. This suggests that, as the isothermal heat-treatment time increased, the phase changed from γ-Alq$_3$ to δ-Alq$_3$.
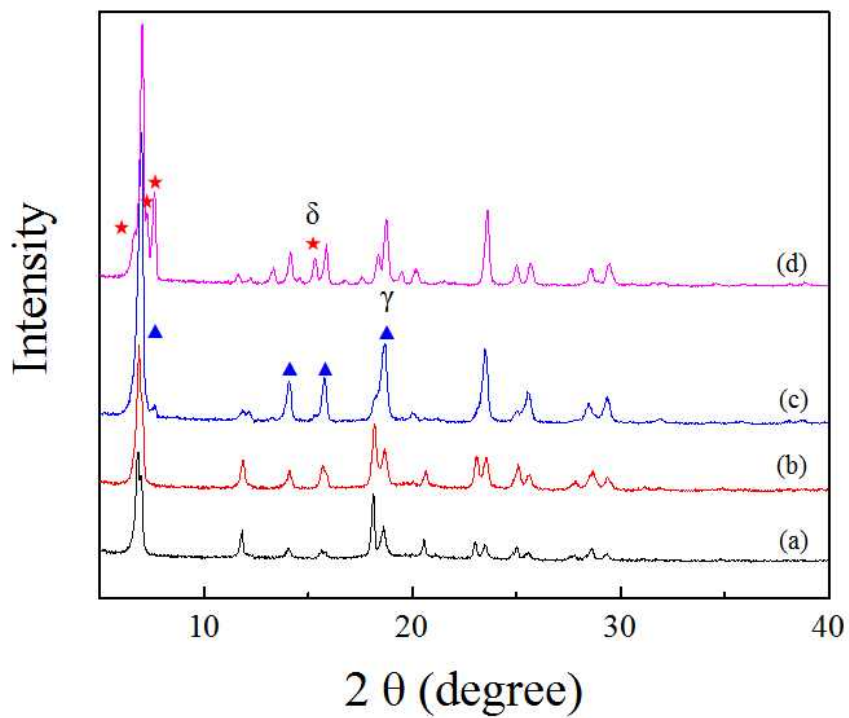
Fig. 48. XRD data of 9 mol% Alq$_3$ crystals obtained over time at the isothermal heat-treatment of 100℃ (a) 1 h, (b) 3 h, (c) 24 h, and (d) 120 h.
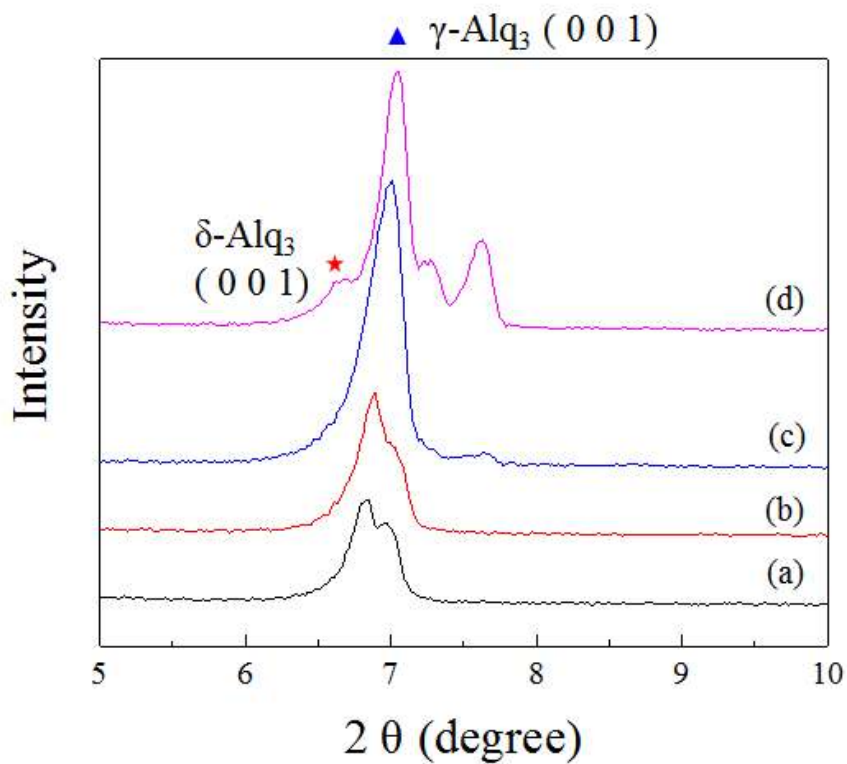
Fig. 49. XRD main peaks data of 9 mol% Alq_3 crystals obtained over time at the isothermal heat-treatment of 100℃ (a) 1 h, (b) 3 h, (c) 24 h, and (d) 120 h.

Fig. 49 shows a schematic of the Alq_3 crystal growth mechanism determined through an analysis of the Alq_3 crystal shape and structure using the $[C_{12}mim][TFSI]$ ionic liquid as the solvent. A study on the growth of ZnO nanorod reported that the crystal growth temperature affects the pH value of the solvent, thus affecting the OH^- ion concentration and the growth shape of the ZnO nanorod crystals [42 ~ 45]. Furthermore, a study conducted in our laboratory on the stability evaluation of ionic liquids reported that the pH value changed to acidic as the temperature of the ionic liquid increased and that this result appears to be due to the deprotonation at the C2-position in the cation structure [25]. Therefore, it is considered that, when the Alq_3 crystals were grown using an ionic liquid as the solvent, as shown in the schematic of the crystal growth mechanism in Fig. 49, the concentration of H^+ ions in the $[C_{12}mim][TFSI]$ solvent increased sharply as the temperature increased from normal to 100℃ in the early stage of crystal growth. Consequently, the (-) charge was concentrated at the tip of the hexagonal-rod and the edge of the crystal growth surface grew first. The middle and late stages of the Alq_3 crystal growth were in the isothermal heat-treatment condition where the crystal growth temperature was maintained at 100℃. The concentration of H^+ ions, which increased sharply in the early stage, was gradually stabilized, the effect of the (-) charge that had been concentrated at the tip of the crystal growth surface decreased, and finally, the solid hexagonal-rod was formed.
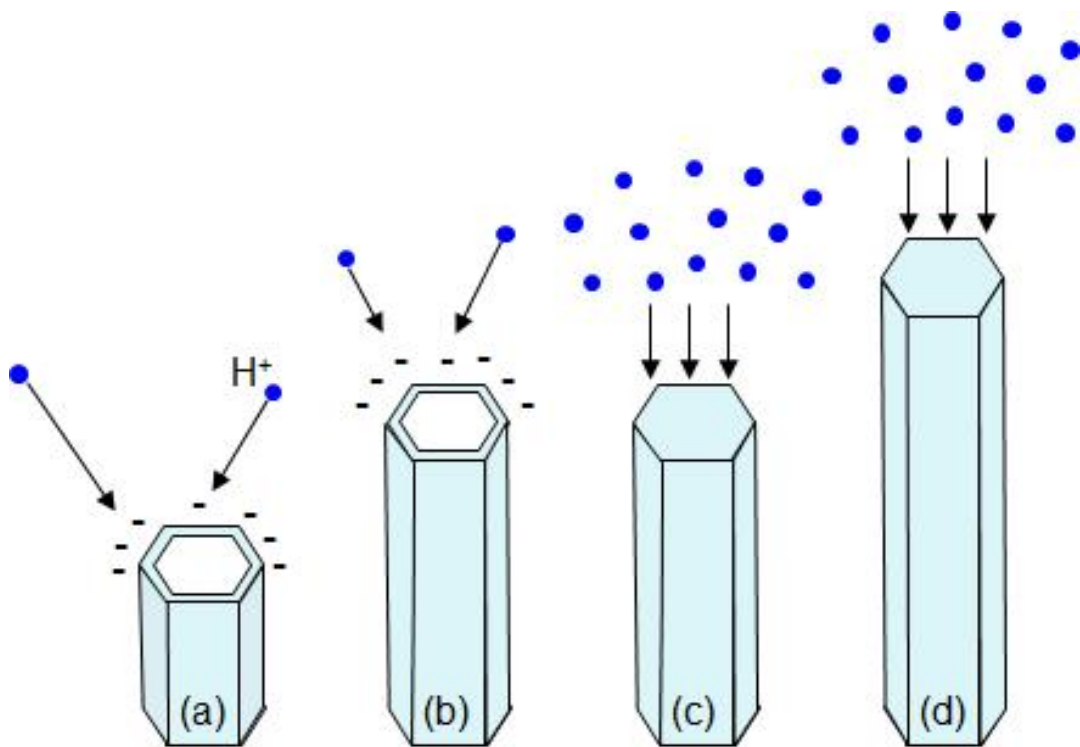
Fig. 50. Crystal growth mechanism of Alq$_3$ crystals grown in the [C$_{12}$mim][TFSI] ionic liquid according to the isothermal heat-treatment time (a) 1 h, (b) 3 h, (c) 24 h, and (d) 120 h.

From the investigation of the crystal growth mechanism, it was considered that the early stage of the Alq$_3$ crystal growth should be examined closely. Thus, to verify the early results of growth, the composition of the Alq$_3$ and [C$_{12}$mim][TFSI] mixture was adjusted to 7 mol%. The results of crystal growth of 7 mol% Alq$_3$ for 6 h at the isothermal heat-treatment temperature of 100℃ are shown in Fig. 50.

In the early stage of crystal growth, the Alq$_3$ crystals showed a needle shape with a length of approximately 20 ㎛, and grew to a hexagonal-rod shape with a length of approximately 30 ㎛ after 6 h. Furthermore, abnormal grain growth, which occurs owing to grain coarsening by 2-D nucleation, can be observed in Fig. 50.

The analysis result for the length growth of Alq$_3$ crystals according to the isothermal heat-treatment time is shown in Fig. 51. From the analysis of Alq$_3$ crystals that grew to the minimum and maximum sizes under each condition and the average size, it was observed that abnormal grain growth appeared after 3 h of isothermal heat-treatment. Owing to the abnormal grain growth, the Alq$_3$ crystals that had undergone heat-treatment for 6 h grew to approximately 80 ㎛.

The impurities of organic materials that have undergone crystal growth via the solution method mainly exist outside the grown crystals. As the crystal size increases, the surface area decreases, and the possibility of impurities also decreases, thus increasing purity. Based on this reasoning, it can be assumed that the larger the size of the grown crystal, the higher the purity will be. As grain coarsening is closely associated with purity, high-purity materials can be produced by growing coarsened grains. Therefore, exploring the conditions of abnormal grain growth is meaningful for this reason.
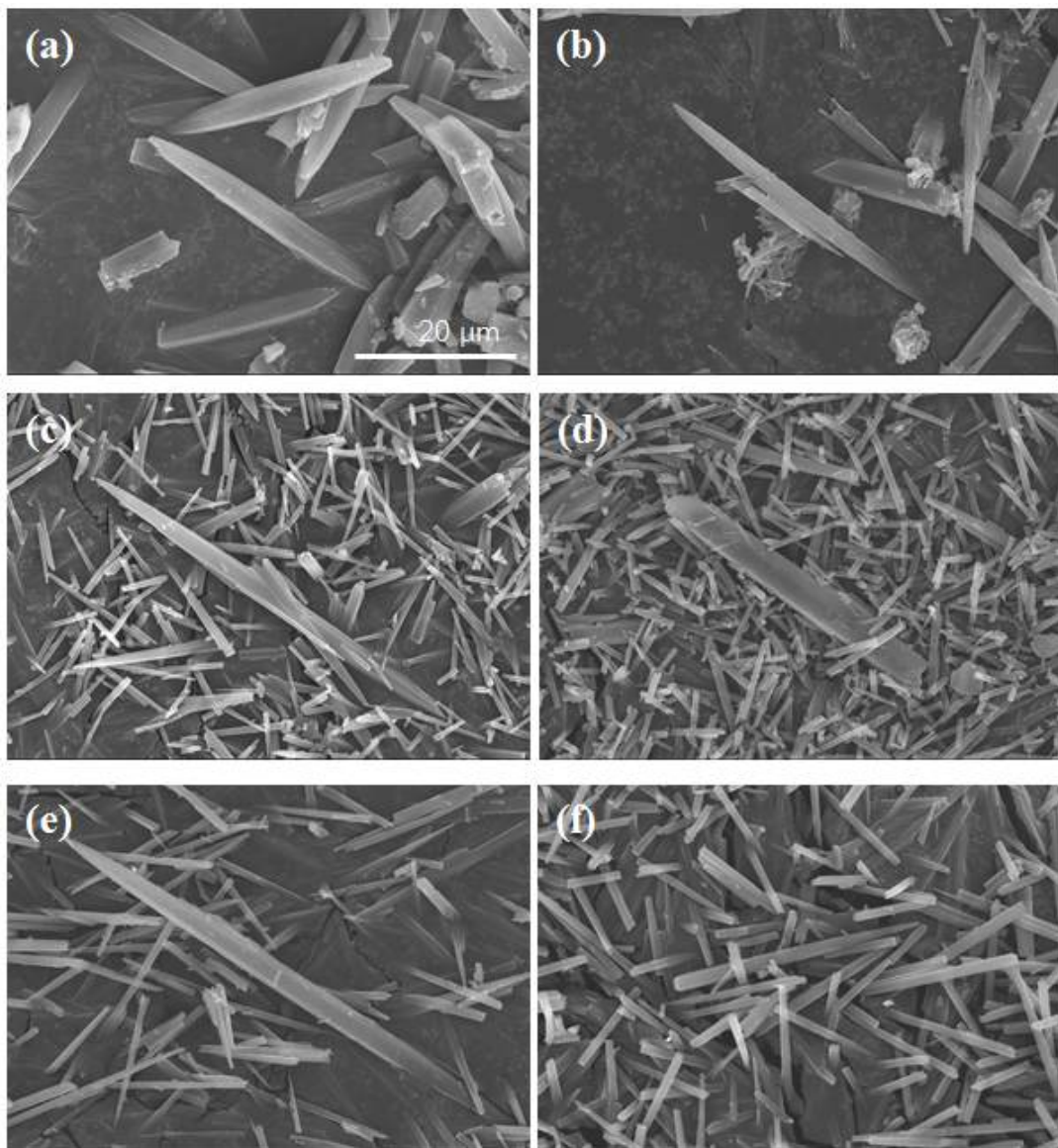
Fig. 51. SEM images of 7 mol% Alq$_3$ crystals obtained over time at the isothermal heat-treatment temperature 100℃ (a) 1 h, (b) 2 h, (c) 3 h, (d) 4 h, (e) 5 h, and (f) 6 h.
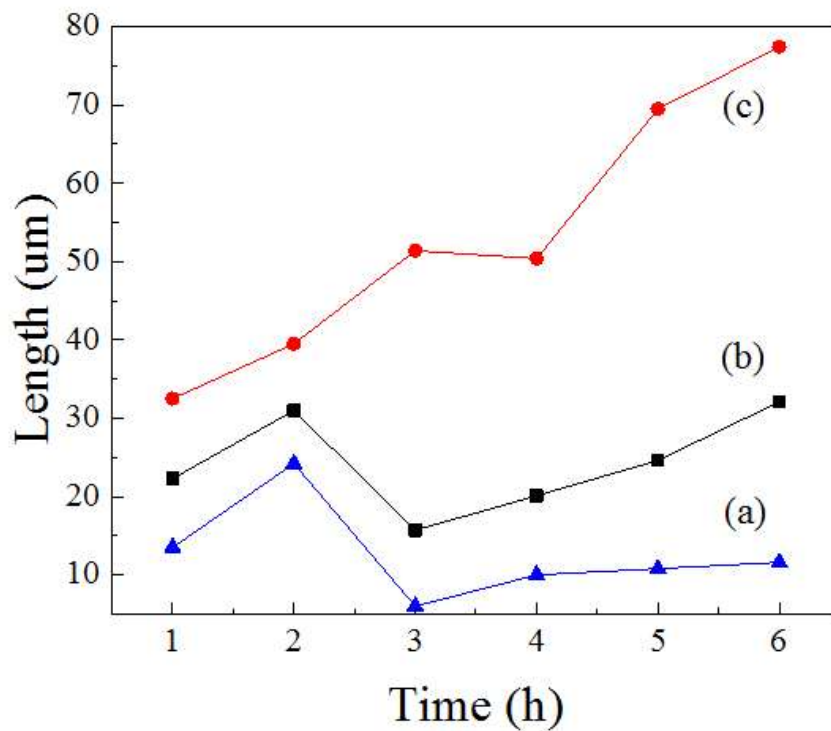
Fig. 52. Length data depending on the isothermal heat-treatment temperature for 7 mol% Alq_3 crystals (a) minimum length, (b) average length, and (c) maximum length.

4. Crystal growth depending on the 2-step growth conditions

Based on the results of abnormal grain growth from the study of the crystal growth mechanism, the experimental conditions for grain coarsening were designed.

Fig. 52 shows the 2-step growth conditions where the Alq_3 is heat-treated at 100℃ for 1 hour and there after at 120℃, 160℃, and 200℃ for 1 hour, and the compositions are 6 mol% and 8 mol%. The SEM images of the Alq_3 crystals obtained under the experimental conditions in Fig. 52 are shown in Fig. 53. Fig. 53 (a) shows the SEM image of the Alq_3 crystal obtained after heat-treatment of 6 mol% Alq_3 for 1 hour at the heat-treatment temperature of 100℃. The length of Alq_3 crystals was measured to be 21.2 ㎛ on average, but as shown in the SEM image in Fig. 53 (a), the difference between the minimum and maximum lengths is large. The minimum and maximum lengths of the grown Alq_3 crystals are 6.8 ㎛ and 46.3 ㎛, respectively. Thus, the length difference of Alq_3 crystals grown under the same conditions was approximately 7 times. Figs. 53 (b) ~ (d) show the SEM images of Alq_3 crystals obtained via heat-treatment of 6 mol% Alq_3 for 1 hour at 120℃, 160℃, and 200℃, respectively, after crystal growth for 1 hour at the heat-treatment temperature of 100℃. Table 1 shows the comparison of the length measurements of Alq_3 crystals.

In addition, the comparison data with the results of a study conducted previously to identify the tendency depending on the heat-treatment temperature and composition are shown in Fig. 54. It can be observed that, at the heat-treatment temperatures of 140℃ or lower, the result of heat-treatment for 3 hours shows no difference from the result of 2-step growth, and at temperatures of 160℃ or higher, the length of the Alq_3 crystals that underwent isothermal heat-treatment for 3 hours grew more. The reason for this appears to be that, in the case of isothermal heat-treatment at 100℃ for 3 hours, the time required for growth after nucleation is relatively longer compared with that under the 2-step growth condition. Furthermore, in the case of heat-treatment at 100℃ for 1 hour followed by heat-treatment at 160℃ and 200℃ for 1 hour among the 2-step growth conditions, it is considered that the critical nuclei generated at 100℃ were dissolved as the heat-treatment temperature increased, which decreased the matrix grain

size. Consequently, the average crystal size became smaller than that of the Alq$_3$ crystals obtained via isothermal heat-treatment at 100℃ for 3 hours.

Fig. 55 shows the grain size distribution of Alq$_3$ crystals obtained from the 2-step grow that 6 mol%. In the case of heat-treatment at 100℃ for 1 hour followed by heat-treatment at 160℃ for 1 hour (Fig. 55 (c)), it can be observed that the crystals grew longer by 4 times than the average growth length of Alq$_3$ crystals, and the grain size distribution graph suggests the occurrence of abnormal grain growth.
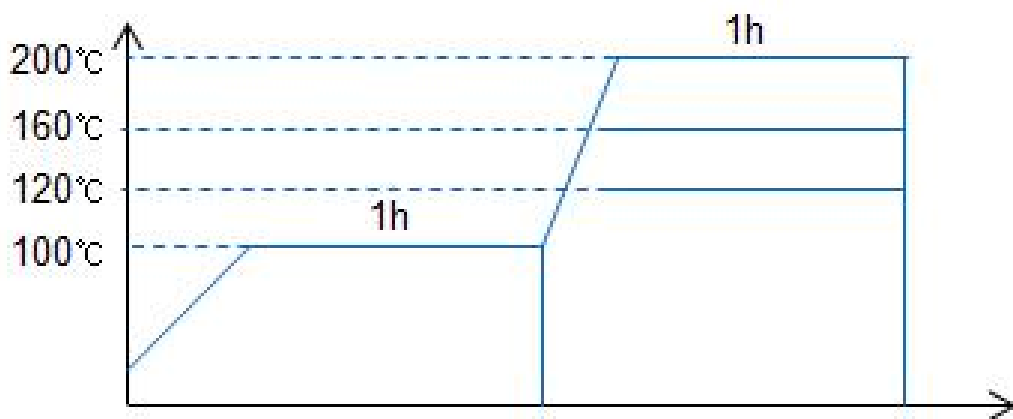
Fig. 53. Experiment conditions for 2-step crystal growth.

Fig. 54. SEM images of (a) 6 mol% Alq$_3$ crystals grown at 100℃ for 1 h, (b) heat-treated at 120℃ for 1 h after at 100℃ for 1 h, (c) heat-treated at 160℃ for 1 h after at 100℃ for 1 h, and (d) heat-treated at 200℃ for 1 h after at 100℃ for 1 h.

μm	average length	maximum length	minimum length
(a) 100℃, 1 h	21.2	46.3	6.8
(b) 100℃, 1 h + 120℃, 1 h	29.5	57.1	10.5
(c) 100℃, 1 h + 160℃, 1 h	23.5	89.1	5.4
(d) 100℃, 1 h + 200℃, 1 h	26.9	70.2	4.1

Table 1. Length comparison data of 6 mol% Alq$_3$ crystals grown under 2-step conditions.
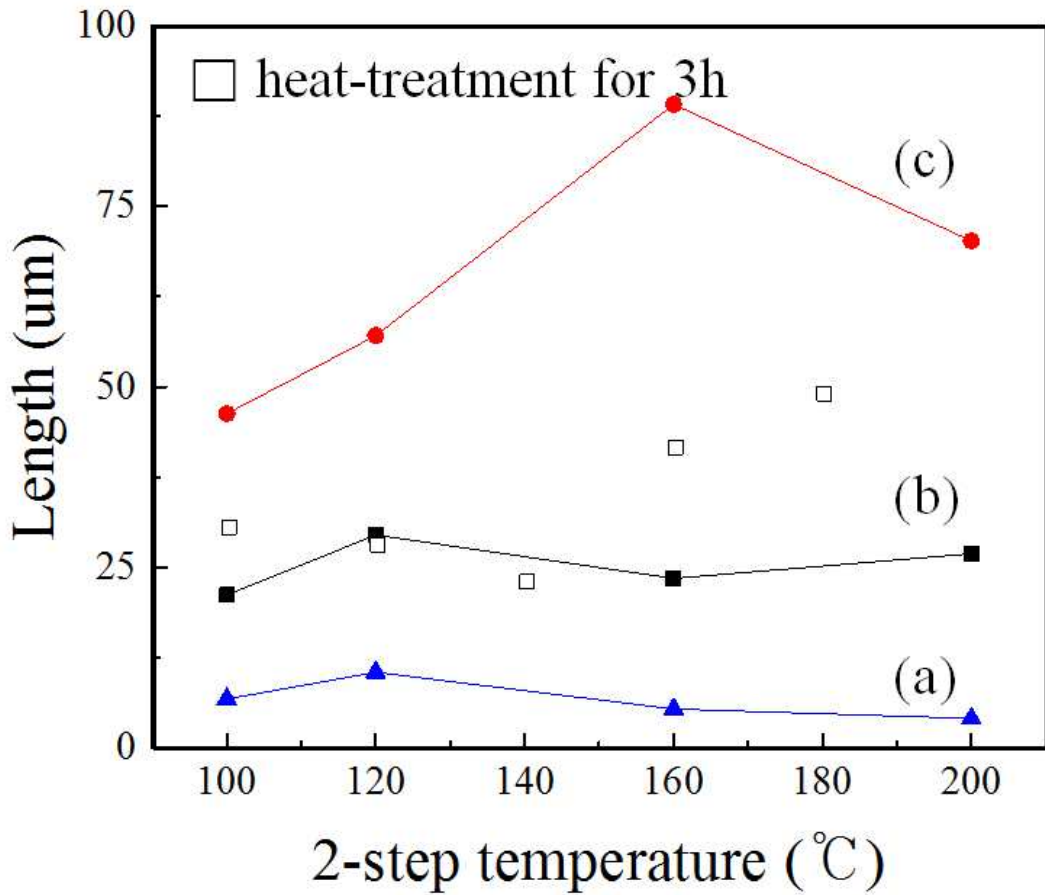
Fig. 55. Length data depending on the 2-step growth condition of 6 mol% Alq$_3$ crystals (a) minimum, (b) average, (c) maximum, and □ isothermal heat-treatment at 100℃ for 3 h.

Fig. 56. The measured crystal size distribution of Alq$_3$ crystals by 2-step growth (a) 6 mol% Alq$_3$ crystals grown at 100℃ for 1 h, (b) heat-treated at 120℃ for 1 h after at 100℃ for 1 h, (c) heat-treated at 160℃ for 1 h after at 100℃ for 1 h, and (d) heat-treated at 200℃ for 1 h after at 100℃ for 1 h.

In abnormal grain growth, as the temperature increases, the threshold critical radius of 2-D nucleation increases, and the minimum grain radius that can be grown by 2-D nucleation decreases compared with the same critical radius. Therefore, in the grain system with a grain size distribution equal to the critical radius, more grains can grow by 2-D nucleation at higher temperatures. This indicates that the number of grains that undergo abnormal grain growth increases at higher temperatures, and the abnormal grain growth theory matches the grain size distribution result under the 2-step growth condition in Fig. 55.

The 2-step growth was also performed at 8 mol%, and the SEM images of the Alq_3 crystals obtained in this experiment are shown in Fig. 56. The average length of the grown Alq_3 crystals was measured to be 20.1 μm, but the minimum and maximum lengths were 8.1 μm and 37.9 μm, respectively. Thus, the difference between the minimum and maximum lengths is approximately more than 4 times. This difference is smaller than that of the 6 mol% composition. A comparison of the measurements of the grown Alq_3 crystals under the 2-step growth conditions is shown in Table 2. In addition, a comparison of these data with the results of the experiment conducted to identify the tendency according to heat-treatment temperature and composition is shown in Fig. 57. In the case of 8 mol% Alq_3, the nuclei growth occurred after the nucleation sites increased already in the early stage of crystal growth. Thus, the average size was similar to that of the Alq_3 crystals grown for 3 hours at the isothermal heat-treatment temperature of 100℃. Fig. 58 shows the grain size distribution of Alq_3 crystals obtained via 2-step grow that 8 mol%. In the case of 8 mol%, the number of grains grown abnormally was already large at 120℃ and as the crystal growth temperature increased, the number of abnormally growing grains became too large, showing anormal grain growth pattern.
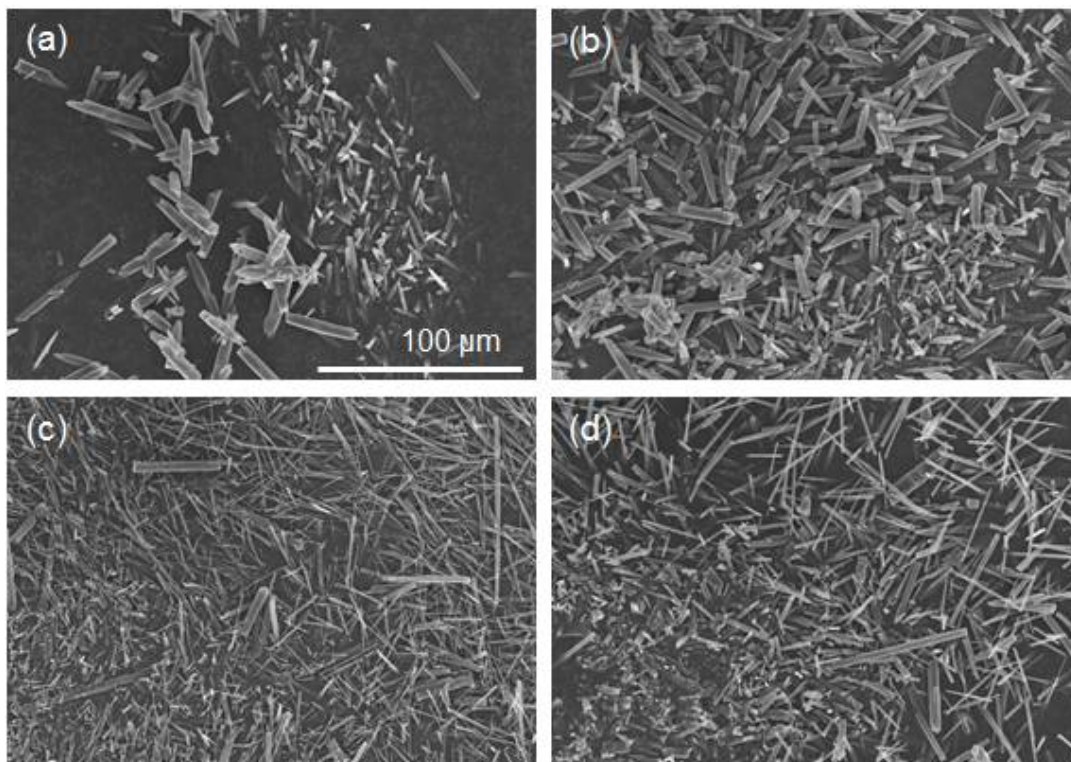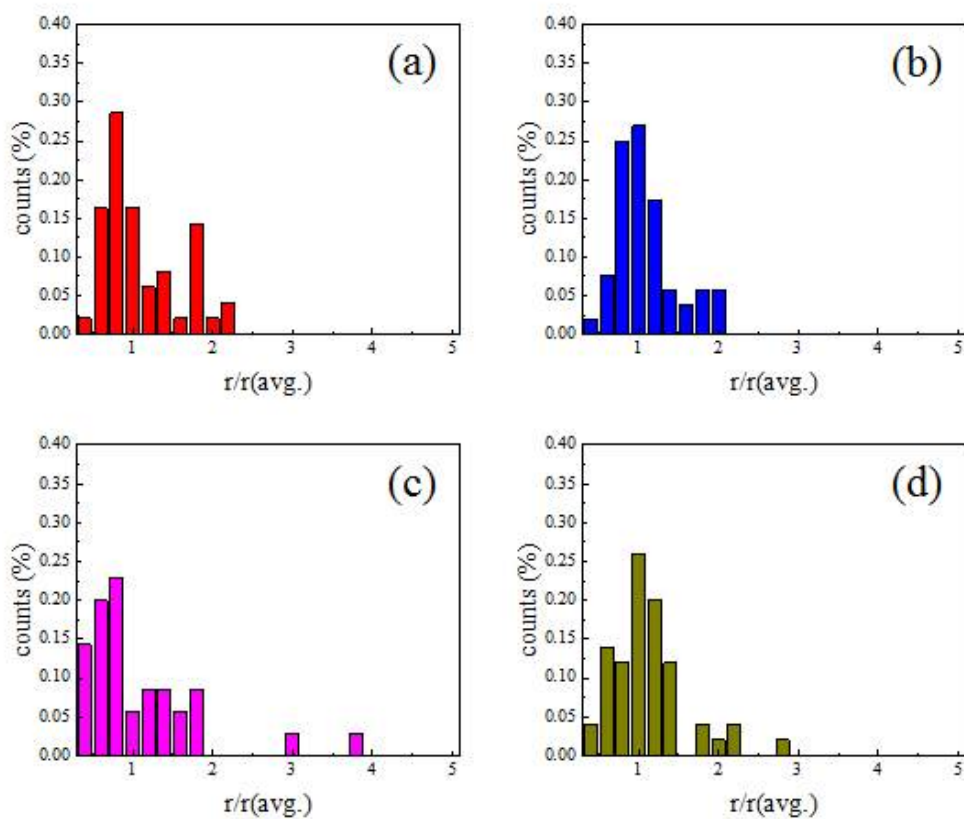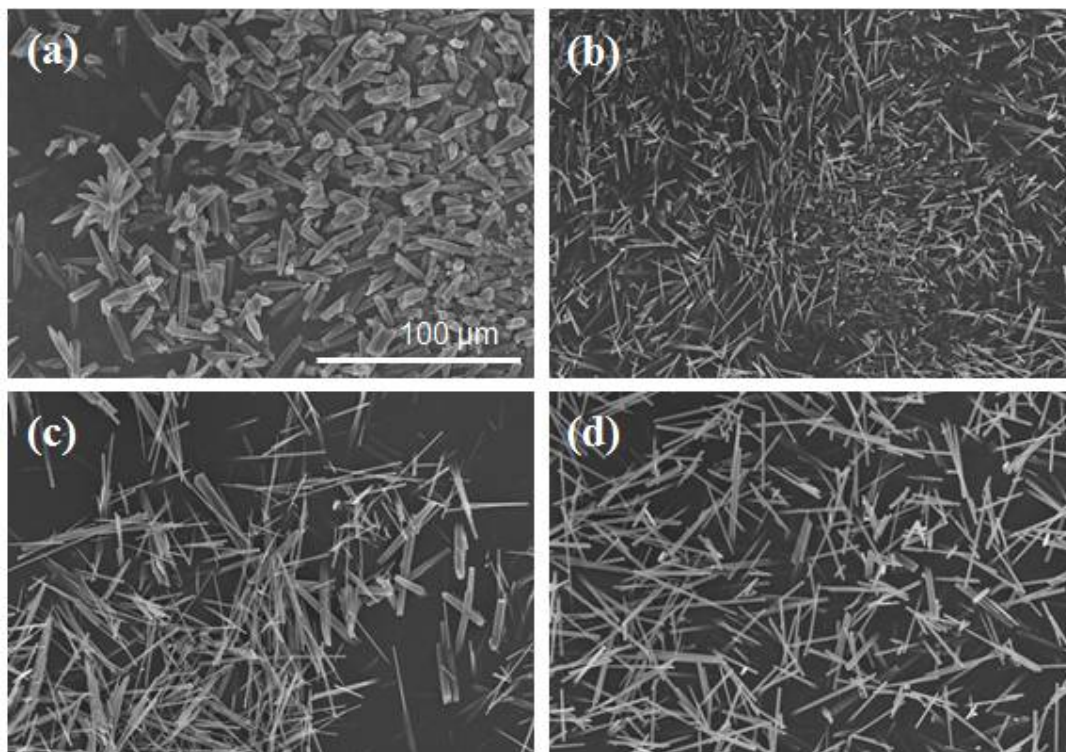
Fig. 57. SEM images of (a) 8 mol% Alq$_3$ crystals grown at 100℃ for 1 h, (b) heat-treated at 120℃ for 1 h after at 100℃ for 1 h. (c) heat-treated at 160℃ for 1 h after at 100℃ for 1 h and (d) heat-treated at 200℃ for 1 h after at 100℃ for 1 h.

μm	average length	maximum length	minimum length
(a) 100℃, 1h	20.1	37.9	8.1
(b) 100℃, 1 h + 120℃, 1 h	18.5	46.2	5.6
(c) 100℃, 1 h + 160℃, 1 h	36.1	61.7	15.4
(d) 100℃, 1 h + 200℃, 1 h	42.2	90.5	19.0

Table 2. Length comparison data of 8 mol% Alq_3 crystals grown under the 2-step conditions.
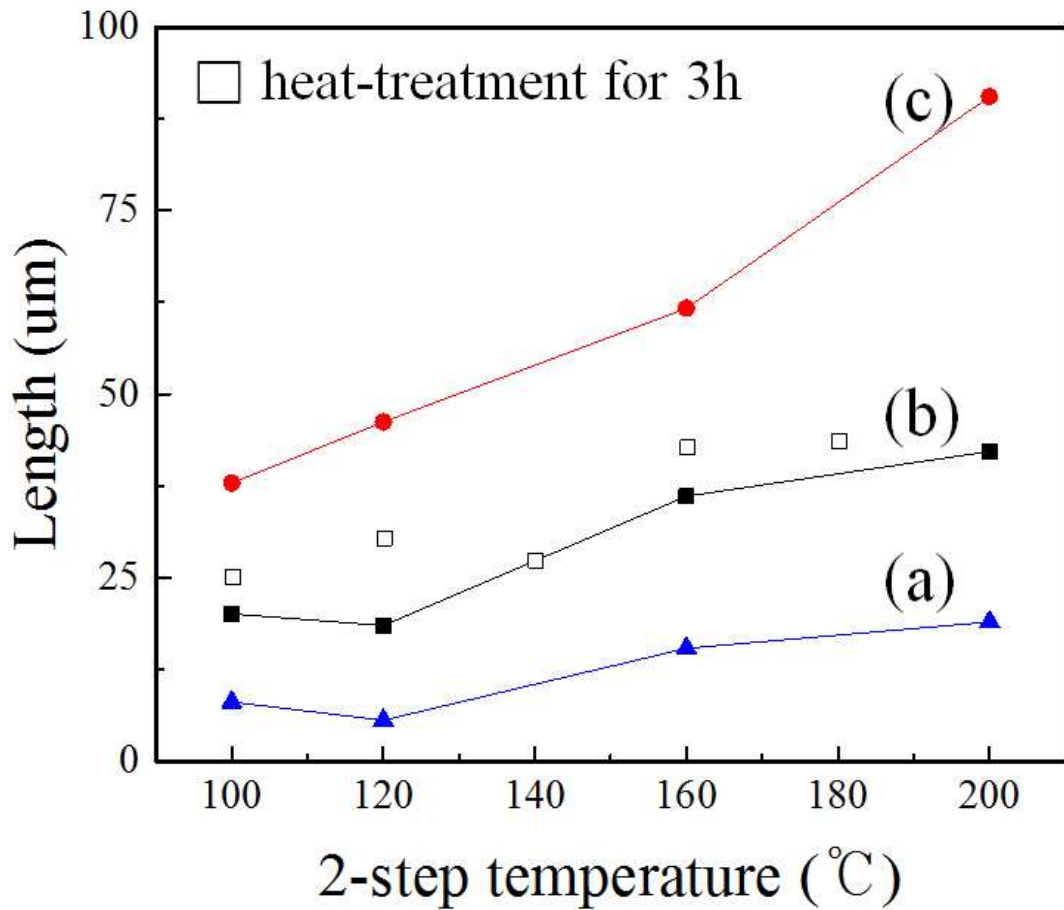
Fig. 58. Length data depending on the 2-step growth conditions of 8 mol% Alq$_3$ crystals. (a) minimum, (b) average, (c) maximum, and □ isothermal heat-treatment at 100℃ for 3 h.
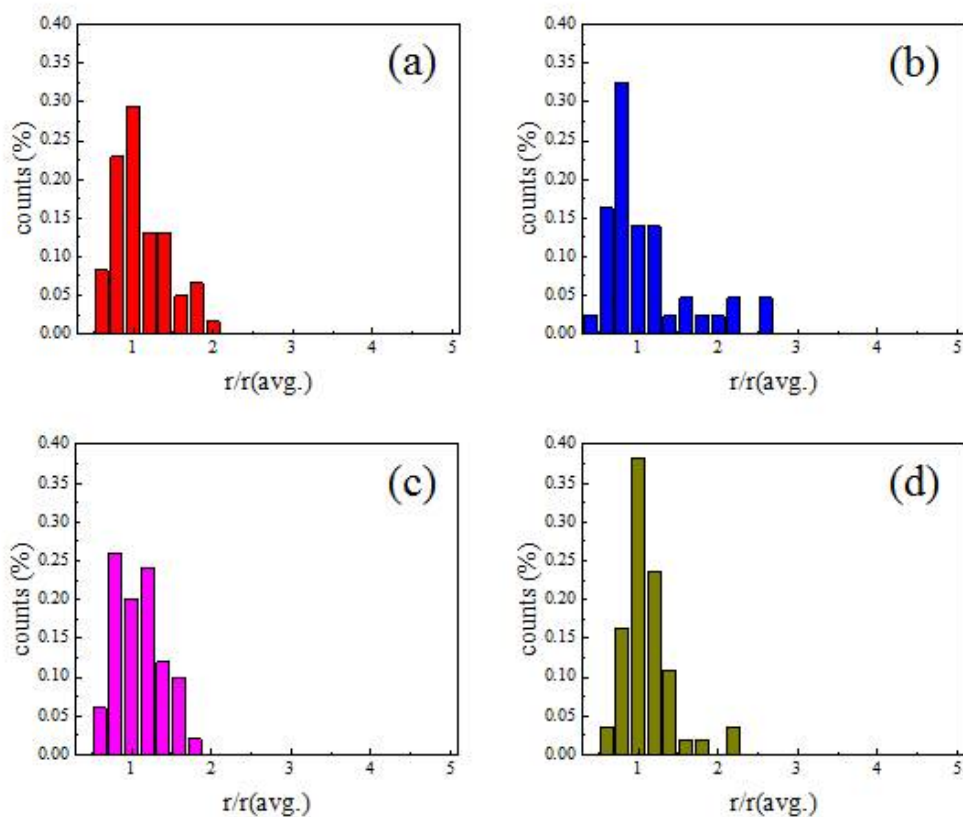
Fig. 59. The measured crystal size distribution of Alq$_3$ crystals by 2-step growth (a) 8 mol% Alq$_3$ crystals grown at 100℃ for 1 h, (b) heat-treated at 120℃ for 1 h after at 100℃ for 1 h, (c) heat-treated at 160℃ for 1 h after at 100℃ for 1 h, and (d) heat-treated at 200℃ for 1 h after at 100℃ for 1 h.

5. Crystal growth depending on the continuous cooling rate

A study was conducted to control the cooling rate after heat-treatment for grain coarsening through abnormal grain growth. Fig. 59 illustrates a graph showing the experimental conditions. The Alq_3 crystals were grown at different cooling rates of 0. 1℃/min, 0.075℃/min and 0.05℃/min after the temperature was increased to 200℃. The heat-treatment times were 16 h 40 min, 22 h 12 min, and 33 h 24 min at each cooling rate, respectively, which are longer than the heat-treatment time of the previous isothermal heat-treatment study. Fig. 60 shows the SEM images of the Alq_3 crystals obtained by raising the temperature of 6 mol% Alq_3 to 200℃ and there after cooling it to 100℃. The graph analyzing the lengths of Alq_3 crystals and the grain size distribution based on Fig. 60 is shown in Fig. 61. Table 3 (b) shows the minimum grain sizes. As the number of growing abnormal grains increases, the base grains are quickly eliminated and the atomic flux received by each abnormal particle is also reduced. Consequently, when all the base grains are eliminated, the critical radius increases sharply as shown in the minimum grain size result in Table 3 (d) and abnormal grain growth stops, confirming convergence to normal grains. The abnormal grain growth stops if the growth driving force is lower than the critical driving force required for 2-D nucleation. To maintain abnormal grain growth, the critical radius of base grains must be maintained small and the flux of dissolved atoms must be supplied to a small number of limited grains. This indicates that only a small number of grains must grow into abnormal grains.
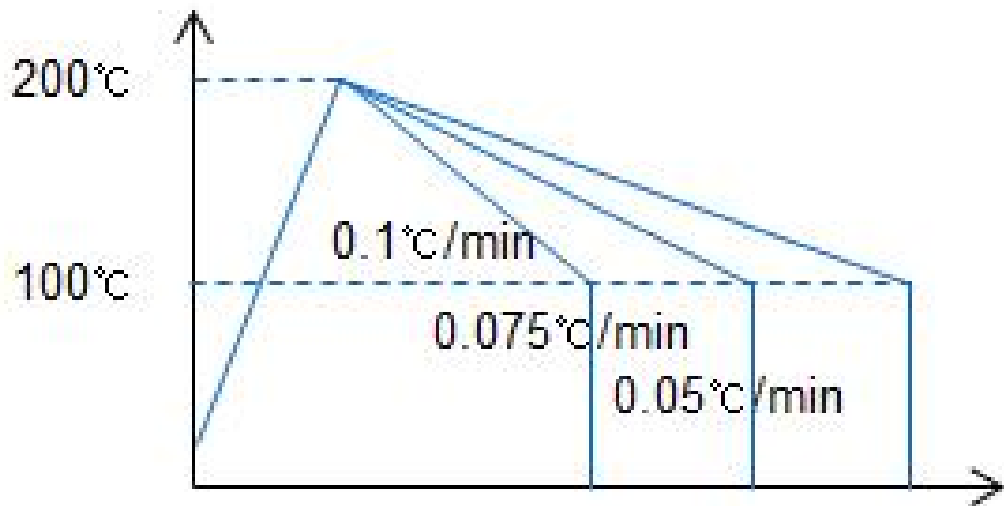
Fig. 60. Experiment conditions for continuous cooling rates.

Fig. 61. SEM images of 6 mol% Alq$_3$ crystals as function of continuous cooling rates (a) 0.1℃/min, (b) 0.075℃/min, and (c) 0.05℃/min.

- 101 -

Fig. 62. Length data & crystal size distribution as function of continuous cooling rates of 6 mol% Alq$_3$ (a) length data, (b) 0.1℃/min, (c) 0.075℃/min, and (d) 0.05℃/min.

μm	average length	maximum length	minimum length
(b) 0.1℃/min	53.8	142.8	27.8
(c) 0.075℃/min	27.3	126.0	6.4
(d) 0.05℃/min	60.1	96.6	30.5

Table 3. Length comparison data of 6 mol% Alq$_3$ crystals grown under different continuous cooling rates.

The SEM images of the Alq_3 crystals obtained under the continuous cooling condition at the 8 mol% composition are shown in Fig. 62. These results confirm the appearance of abnormal grain growth under all conditions. Fig. 63 shows a graph analyzing the lengths of Alq_3 crystals and a grain size distribution graph under different cooling conditions at the 8 mol% composition. It is considered that, even if large abnormal grains are grown, a large driving force for growth can be supplied to the growing abnormal grains and the abnormal grain growth can be continued because the number of abnormally growing grains is small and the small critical radius is maintained to the base grain size. Table 4 (b) shows that the maximum size of Alq_3 crystals obtained through continuous cooling is 176.4 ㎛. This is approximately twice as large as the size of Alq_3 crystals obtained through the conventional solution method, and the purity must have improved as a result. Furthermore, the number of abnormally growing grains increased from Table 4 (c) to (d). From this result, it is estimated that the Alq_3 crystals obtained at a cooling rates lower than 0.05℃/min will converge to normal grains.
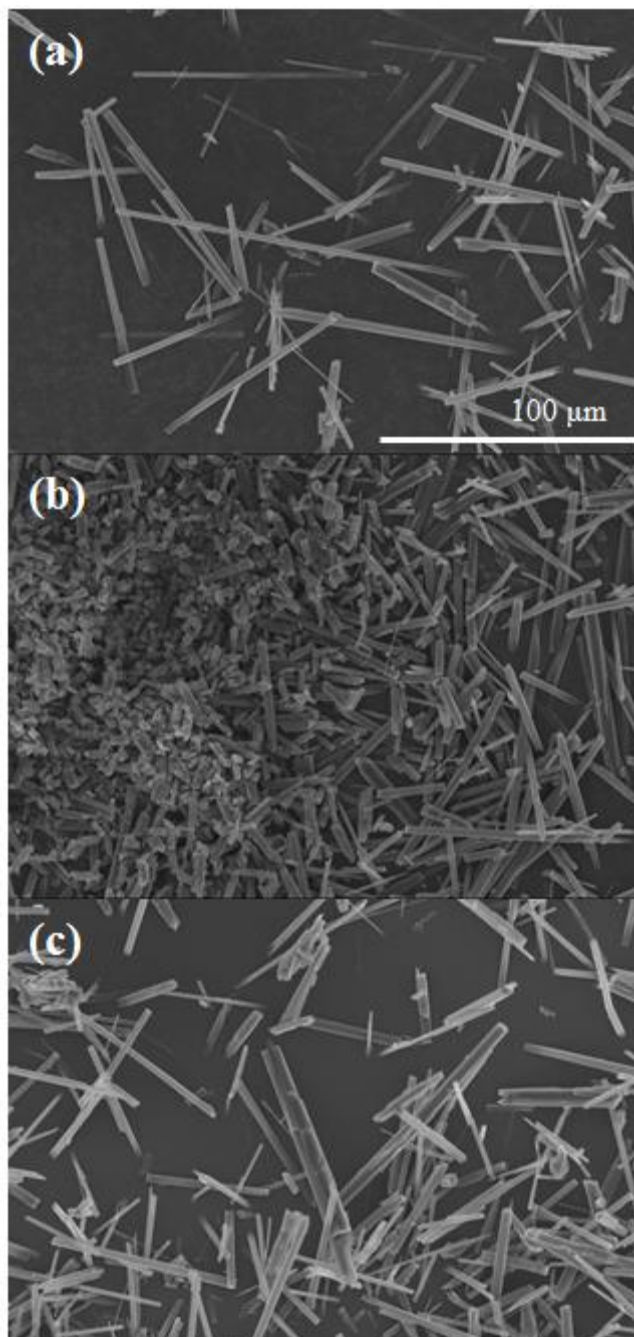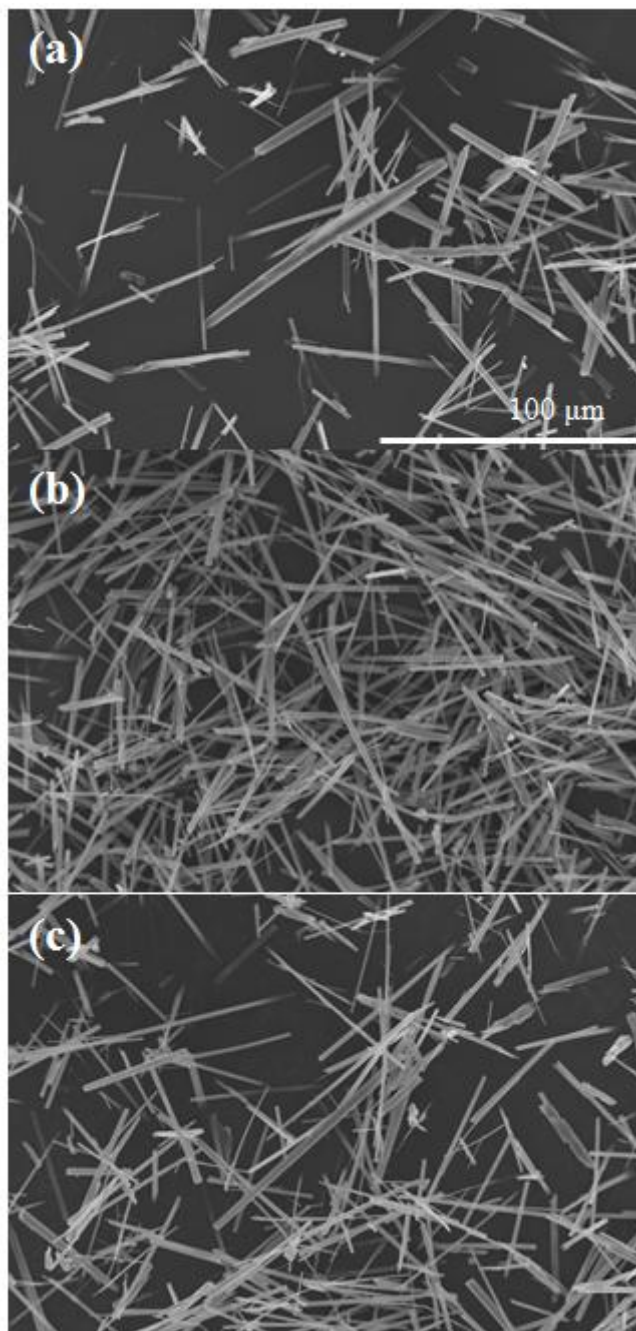
Fig. 63. SEM images of 8 mol% Alq$_3$ crystals as function of continuous cooling rates (a) 0.1℃/min, (b) 0.075℃/min, and (c) 0.05℃/min.
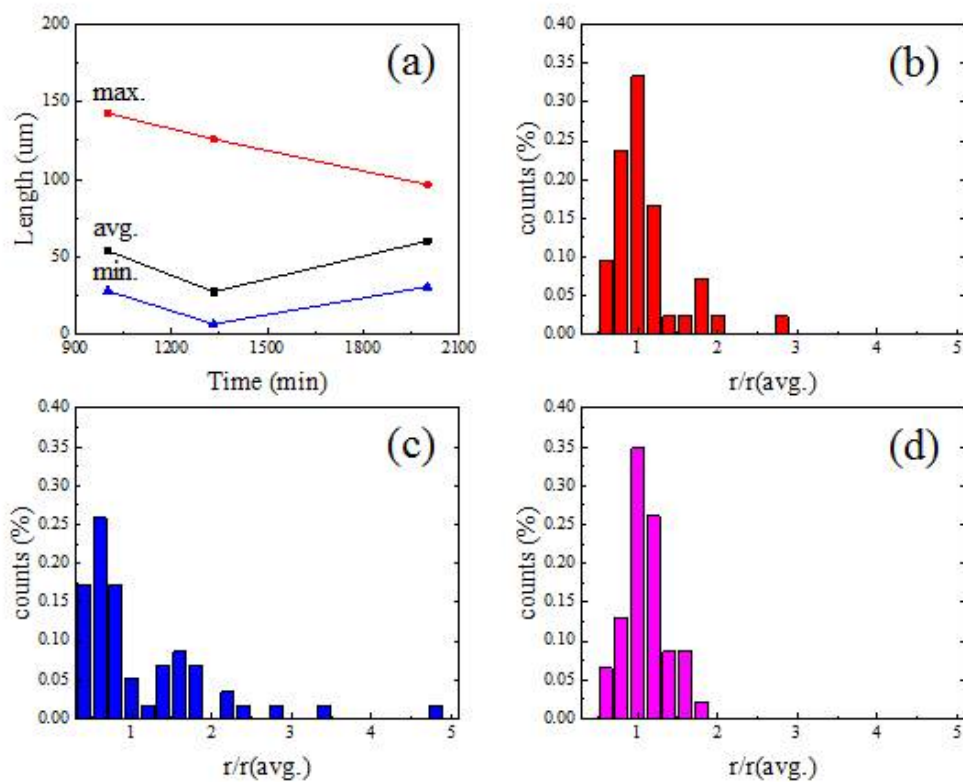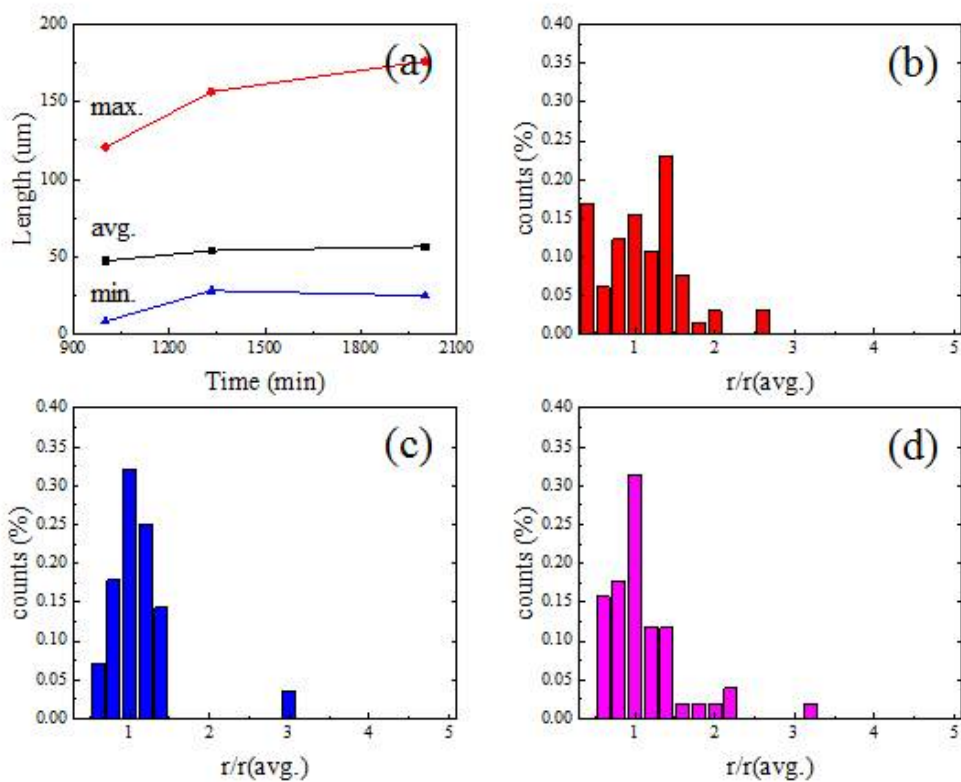
Fig. 64. Length data & crystal size distribution as function of continuous cooling rates of 8 mol% Alq₃ (a) length data, (b) 0.1℃/min, (c) 0.075℃/min, and (d) 0.05℃/min.

μm	average length	maximum length	minimum length
(b) 0.1℃/min	47.3	120.8	8.1
(c) 0.075℃/min	53.8	156.6	28.0
(d) 0.05℃/min	56.4	176.4	24.6

Table 4. Length comparison data of 8 mol% Alq_3 crystals grown under different continuous cooling rates.

V. CONCLUSIONS

The crystal growth of Alq_3, which is are presentative OLED material, was investigated using the solution method with the $[C_{12}mim][TFSI]$ ionic liquid as the solvent. The results of analysis of Alq_3 crystals grown in the mixed solution of $[C_{12}mim][TFSI]$ ionic liquid and Alq_3 depending on the heat-treatment temperature and composition confirmed that, as the heat-treatment temperature increased from 100℃ to 180℃, the growth shape changed to the equilibrium shape. The XRD measurement results confirmed that, as the heat-treatment temperature increased, the phase changed from γ-phase to δ-phase. Furthermore, pure δ-Alq_3 could be obtained when 16 mol% Alq_3 crystals were grown at the heat-treatment temperature of 180℃. The conventional solution method used to grow Alq_3 crystals is harmful and complex because it uses a highly toxic solvent and additives such as surfactant are used. However, the solution method used in this study is safe and simple because it only uses an environmentally friendly ionic liquid as the solvent for the solution method with no additives. Thus, the proposed solution method is expected to be applicable to the mass production process.

The Alq_3 crystal growth mechanism in the $[C_{12}mim][TFSI]$ ionic liquid is considered to grow crystals from a hollow hexagonal-rod to a solid structure as the cross section of the hexagonal-rod grows first according to the changing concentration of H^+ ions in the ionic liquid during the heat-treatment process. It is believed that a production process for single-crystals can be developed by investigating the growth mechanism of Alq_3 crystal in the $[C_{12}mim][TFSI]$ ionic liquid, which will enable the production of organic single-crystals with improved crystallinity.

As the purity of Alq_3 crystals grown via the solution method increases as the crystal size grows, the abnormal grain growth conditions for grain coarsening were explored, and Alq_3 crystals of size 176 ㎛ were obtained by growing crystals at the cooling rate of 0.05℃/min from the heat-treatment temperature of 200℃ to 100℃. This new solution method is expected to provide higher purity because it can grow Alq_3 crystals with approximately double the size of the Alq_3 crystals grown via the conventional solution method.

It is believed that mass production of highly pure Alq_3 single-crystals can be achieved through the solution method using an ionic liquid as a solvent. Thus, it is expected that, in the near future, we can freely use center information displays providing driving information and entertainment, window displays, and flexible and rollable displays with improved portability, design, and convenience in everyday life. Furthermore, the results of research on the Alq_3 crystal growth mechanism in ionic liquids will contribute to the development of related fields in the future.

[Reference]

1. H. Jiang, and C. Kloc, *MRS BULLETIN*, **38**, (2013) 28-33.

2. C. Reese, and Z. Bao, *materialstoday*, **10**, (2007) 20-27.

3. K. Fukuda, K. Hikichi, T. Sekine, Y. Takeda, T. Minamiki, D. Kumaki, and S. Tokito, *Scientific Reports*, **3**, (2013) 2048-2054.

4. J. Zhang, L. Zhu, and Z. Wei, *small methods*, **1**, (2017) 1700258.

5. T. Lei, and J. Pei, *J. Mater. Chem.*, **22**, (2012) 785-798.

6. Y. D. Park, Y. Jang, H. H. Choi, and K. Cho, *Prospectives of Industrial Chemistry*, **11**, (2008) 30-46.

7. I. Kang, H.-J. Yun, D. S. Chung, S.-K. Kwon, and Y.-H. Kim, *J. Am. Chem. Soc.*, **135**, (2013) 14896-14899.

8. H. -R. Tseng, H. Phan, C. Luo, M. Wang, L. A. Perez, S. N. Patel, L. Ying, E. J. Kramer, T.-Q. Nguyen, G. C. Bazan, and A. J. Heeger, *Adv. Mater.*, **26**, (2014) 2993-2998.

9. C. Luo, A. K. K. Kyaw, L. A. Perez, S. Patel, M. Wang, B. Grimm, G. C. Bazan, E. J. Kramer, and A. J. Heeger, *Nano Letters*, **14**, (2014) 2764-2771.

10. J. -S. Hu, H. -X. Ji, An.-M. Cao, Z. -X. Huang, Y. Zhang, L. -J. Wan, A. -D. Xia, D. -P. Yu, X. -M. Meng, and S. -T. Lee, *Chem. Commun.*, **0**, (2007) 3083-3085.

11. Y. -T. Oh and D. -C. Shin, *Journal of Crystal Growth*, **487**, (2018) 78-82.

12. J. Polte, *Cryst. Eng. Comm.*, **17**, (2015) 6809-6830.

13. T. Kimura, Advances in Ceramics - Synthesis and Characterization, Processing and Specific Applications, *InTech*, **09**, (2011) 75-100.

14. I. Sunagawa, *Forma*, **14**, (1999) 147-166.

15. K. G. Libbrecht, *Rep. Prog. Phys.*, **68**, (2005) 855-895.

16. J. Zhang, F. Huang and Z. Lin, *Nanoscale*, **2**, (2010) 18-34.

17. Y. J. Park, N. M. Hwang, and D. Y. Yoon, *Metallurgical and Materials Transactions A*, **27A**, (1996) 2809-2819.

18. R. Warren and M. B. Waldron, *Powder Metall.*, **15**, (1972) 166-201.

19. C.W. Tang, and S.A. VanSlyke, *Appl. Phys. Lett.*, **51**, (1987) 913-915.

20. M. Brinkmann, G. Gadret, M. Muccini, C. Taliani, N. Masciocchi, and A. Shroni, *J. Am., Chem., Soc.*, **122**, (2000) 5147-5157.

21. M. Cölle, R. E. Dinnebier, and W. Brütting, *Chem. Commun.*, **0**. (2002) 2908-2909.

22. M. Rajeswaran, and T. N. Blanton, *Journal of Chemical Crystallography*, **35**, (2005) 71-76.

23. M. Rajeswaran, T. N. Blanton, C. W. Tang, W. C. Lenhart, S. C. Switalski, D. J. Giesen, B. J. Antalek, T. D. Pawlik, D. Y. Kondakov, N. Zumbulyadis, amd R. H. Young, *Polyhedron*, **28**, (2009) 835-843.

24. C. Maton, N. D. Vos, and C. V. Stevens, *Chem. Soc. Rev.*, **42**, (2013) 5963-5977.

25. K. -H. Kim, S. -W. Choi, S. -Y. Park, Y. -T. Oh, and D. -C. Shin, *Journal of Advanced Engineering and Technology*, **9**, (2016) 171-176.

26. S. S. Mondal, H. Müller, M. Junginger, A. Kelling, U. Schilde, V. Strehmel, and H. -J. Holdt, *Chem. Eur. J.*, **20**, (2014) 8170-8181.

27. P. Wasserscheid, and T. Welton, Ionic liquids in Synthesis (2nd Edition), *WILEY-VCH* (2007).

28. P. Bonhôte, A. -P. Dias, N. Papageorgiou, K. Kalyanasundaram, and M. Grätzel, *Inorg. Chem.*, **35**, (1996) 1168-1178.

29. A. B. McEwen, H. L. Ngo, and K. LeCompte, J. L. Goldman, *J. Electrochem. Soc.*, **146**, (1999). 1687-1695

30. H. Matsumoto, M. Yanagida, K. Tanimoto, M. Nomura, Y. Kitagawa, and Y. Miyazaki, *Chem. Lett.*, **29**, (2000) 922-923.

31. H. Matsumoto, H. Kageyama, and Y. Miyazaki, *Chem. Comm.*, **16**, (2002) 1726-1727.

32. J. M. Crosthwaite, M. J. Muldoon, J. K. Dixon, J. L. Anderson, and J. F. Brennecke, *J. Chem. Thermodynam.*, **37**, (2005) 559-568.

33. J. G. Huddleston, A. E. Visser, W. M. Reichert, H. D. Willauer, G. A. Broker, and R. D. Rogers, *Green Chem.*, **3**, (2001) 156-164.

34. O. O. Okoturo, and T. J. VaderNoot, *J. of Electroanal. Chem.*, **568**, (2004) 167-181.

35. S. H. Lee, and S. B. Lee, *Chem. Commun.*, **0**, (2005) 3469-3471.

36. W. Chen, Q. Peng, and Y. Li, *Adv. Mater.*, **20**, (2008) 2747-2750.

37. W. Xie, H. Song, J. Fan, F. Jiang, H. Yuan, S. Zhang, Z. Wei, Z. Pang, and S. Han, *RSC Adv.*, **5**, (2015) 95405-95409.

38. M. Cölle, J. Gmeiner, W. Milius, H. Hillebrecht, and W. Brütting, *Adv. Funct. Mater.*, **13**, (2003) 108-112.

39. F. -H. Kao, K. -Y. Lin, D. -J. Jan, S. -J. Tang, C. -C. Yang, C. -H. Lin, H. -M. Yeh, and K. -C. Chiu, *Journal of Crystal Growth*, **357**, (2012) 9-14.

40. M. Cölle, and W. Brütting, *Phys. stat. sol. (a)*, **201**, (2004) 1095-1115.

41. T. Fukushima, and H. Kaji, *Organic electronics*, **13**, (2012) 2985-2990.

42. K. -W. Chae, Q. Zhang, J. S. Kim, Y. -H. Jeong, and G. Cao, *Beilstein J. Nanotechnol.*, **1**, (2010) 128-134.

43. F. Li, Y, Ding, P, Gao, X, Xin, and Z, L. Wang, Angew, *Chem. Int. Ed.*, **43**, (2004) 5238-5242.

44. A. Wei, X. W. Sun, C. X. Xu, Z. L Dong, Y. Yang, S. T. Tan and W. Huang, *Nanotechnology*, **17**, (2006) 1740-1744.

45. J. Wang, S. Hou, L. Zhang, J. Chen, and L. Xiang, *Cryst. Eng. Comm.*, **16**, (2014) 7115-7123.